Arabian Journal of Geosciences (2019) 12: 289
https://doi.org/10.1007/s12517-019-4453-6

ORIGINAL PAPER

Geology and petrology of the potassic and ultrapotassic rocks from the northern part of Senirkent (Isparta-SW Turkey): evidence of magma–carbonate wall-rock interactions

Ömer Elitok[1]

Received: 8 January 2019 / Accepted: 1 April 2019 / Published online: 24 April 2019

Abstract
Potassic, ultrapotassic lava domes, flows, and volcano-sedimentary deposits including leucite-bearing and leucite-free grains crop out to the north of Senirkent (Isparta), at the apex of the Isparta Angle (southwestern Turkey). Ultrapotassic rocks are nepheline-foidolite, italite, leucitite, melilite leucitite, melilite-gehlenite leucitite, diopside leucitite, and leucitophyre with lowest SiO_2 content (38.71–44.72 wt%, but the leucitophyre has 51.4 wt%), higher K_2O (4.36–10.19 wt%), MgO (3.25–6.98 wt%), and K_2O/Na_2O ratio (2.65–32.8). Potassic rocks are phonolitic leucitites, sanidine-phyric phonolite, and trachytes with SiO_2 (49.35–64.46 wt%), K_2O (8.28–11.38 wt%), MgO (0.17–1.39 wt%), and K_2O/Na_2O ratio (2.25–11.8). Some leucitites, diopside leucitites, and phonolitic leucitites enclose partly carbonatite occurences or associated with carbonate-rich part including carbonatite globules, phlogopite, clinopyroxene, and/or leucite, melanite crystals embedded in glassy volcanic matrix and/or carbonate matrix. Primitive mantle-normalized incompatible element patterns display strong enrichments in LILEs (Cs, Rb, Ba, U, Th, Sr) relative to HFSEs (Nb, Ti) with distinct negative Nb–Ti anomalies, suggesting subduction-related lavas. Chondrite-normalized REE patterns are characterized by light REE enrichment (251–493 times chondrite for La) and flat heavy REE patterns (10–27 times chondrite for Yb). All the leucite-bearing and leucite-free rocks display similar, subparallel chondrite-normalized and primitive mantle-normalized trace element patterns, suggesting cogenetic origin. Mineralogical, petrological, and geochemical data suggest magma–carbonate wall-rock interaction and tapping of different parts of the melts within the magma chamber along the fault lines formed during neotectonic period and extension-related block faulting.

Keywords Potassic · Alkaline · Carbonatite · Leucite · Italite · Isparta

Introduction

The genesis of potassic and ultrapotassic rocks, magma–carbonate rock interactions, and occurence of carbonatites associated with saturated and undersaturated alkaline volcanic rocks from different regions and tectonic settings have been of interest to petrologists in terms of understanding evolution of K-rich silica-deficient magmas (Freda et al. 1997; Cioni et al. 1998; Shaw 2018). Carbonatitic magma may be generated either directly in the mantle or by differentiation at a much shallower depth (Wooley 2003). Another common suggestion is that carbonatite may form by magma–carbonate wall-rock interaction and melting of crustal carbonate rocks (Freda et al. 1997; Mollo et al. 2010; Pichavant et al. 2014; Shaw 2018). Especially, some volcanic provinces such as Roman Volcanic Province within central Italy (Peccerillo 1998), eastern Paraguay, Brazil in the central South America, Angola, Namibia, and Zimbabwe in the South Africa (Comin-Chiaramonti et al. 2007) have gained much attention in this respect. Potassic igneous rocks are defined by molar K_2O/Na_2O ratio of about or higher than unity. Ultrapotassic rocks have higher K_2O, MgO content (> 3 wt%), and K_2O/Na_2O ratio > 2 for whole rock analyses (Foley et al. 1987). These kind of rocks may be formed at different tectonic settings (e.g., convergene plate margins (orogenic), post-collisional extensional tectonic settings,

Editorial handling: F. Lucci

✉ Ömer Elitok
oelitok@gmail.com

[1] Department of Geological Engineering, Suleyman Demirel University, 32260 Isparta, Turkey

stabil within plates subjected to extensional tectonic regime) (Peccerillo et al. 1984; Poli et al. 1984; Beccaluva et al. 1991; Nelson 1992; Van Bergen et al. 1992).

North-south trending volcanic rocks crop out from the apex of the Isparta Angle (Gölcük volcano, Isparta) to the north of Afyon (Kırka area) including the study area. This volcanic area is called Kırka-Afyon-Isparta Volcanic Province (KAIVP, Francalanci et al. 2000) or Kırka-Afyon-Isparta Alkaline Volcanic assemblage (KAIAV, Savaşçın and Oyman 1998), but this volcanic area will be hereafter referred as Kırka-Afyon-Isparta Volcanic Province (KAIVP, Fig. 1). Geology, petrography, isotope, whole rock and mineral chemistry, geochronology, and genesis of the volcanic rocks of the KAIVP have been investigated by domestic and foreign researchers (Alıcı et al. 1998; Savaşçın and Oyman 1998; Francalanci et al. 2000; Akal 2003, 2008; Aydar et al. 2003; Platevoet et al. 2008, 2014 Elitok et al. 2010; Akal et al. 2013). In general, volcanic activity is younger in the Isparta region (4.7 ± 02 Ma (Lefèvre et al. 1983), 24 ± 2 ka (Platevoet et al. 2008), and 12.9 ± 0.4 ka (Schmitt et al. 2014) than the Kırka-Afyon region (between 8.6 and 14.8 Ma, Francalanci et al. 2000), suggesting that the volcanics in the KAIVP were emplaced at different times younging from north (Kırka area) to the south (Isparta area).

This study aimed to investigate field relations, petrographic and whole rock geochemical characteristics of the volcanic rocks occuring as lava extrusions and their clasts within the volcano-sedimentary deposits in the north of Senirkent which occurs within the north-south trending KAIVP in the south-west Turkey. Also, carbonatite occurences are associated with potassic and ultrapotassic igneous rocks in the study area. Evolution of the potassic and ultrapotassic rocks and their relationship with carbonatite occurences in the study area were discussed, and a new perspective was brought in terms of evolution of the potassic and ultrapotassic igneous rocks.

Geology

Regional geological setting

Southern Turkey is characterized mainly by east-west trending carbonate axis (Tauride carbonate axis), and the western part of the Tauride carbonate axis forms a north-pointing cusp at the Senirkent area in southwestern Turkey, so-called Isparta Angle (Fig. 2). Northeast-southwest trending Beydağları platform carbonate rocks (western limb of the Isparta Angle) and northwest-southeast trending Anamas-Akseki platform carbonate rocks (eastern limb of the Isparta Angle) separate

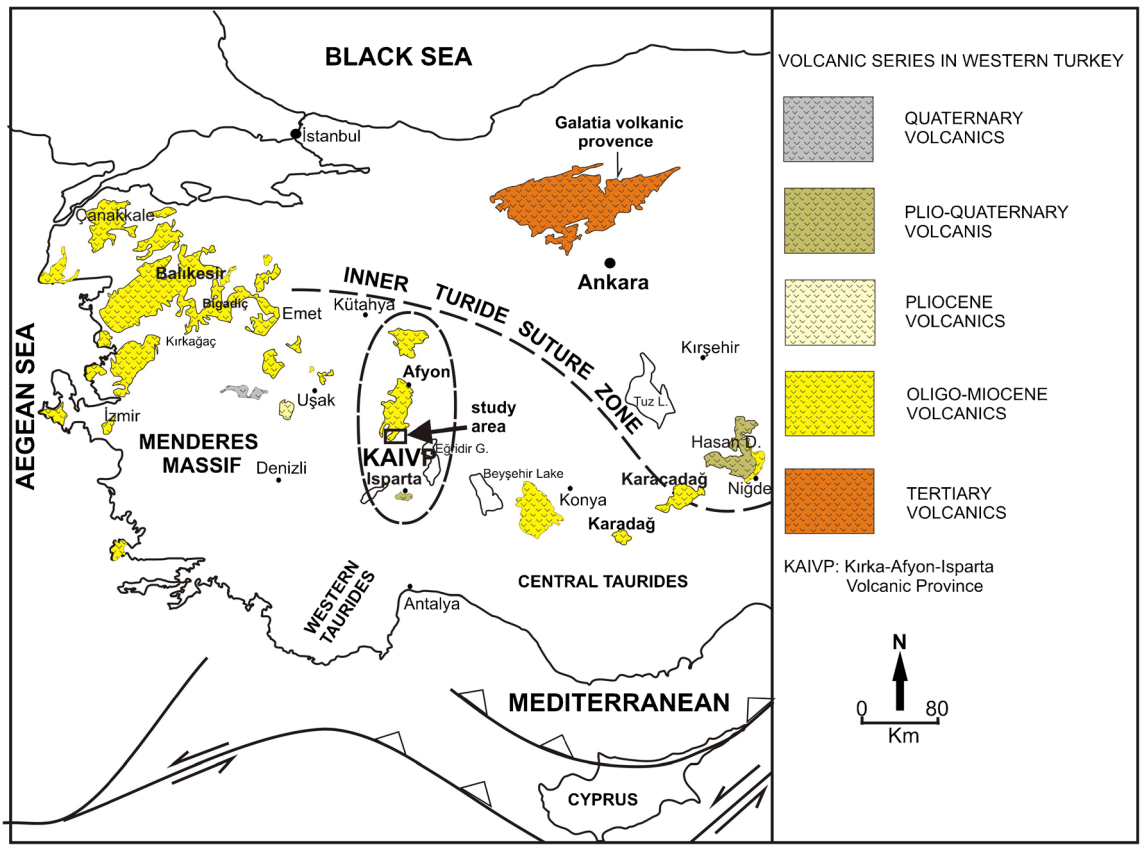

Fig. 1 Distribution of Cenozoic volcanics in central and western Turkey (simplified from Bingöl 1989)

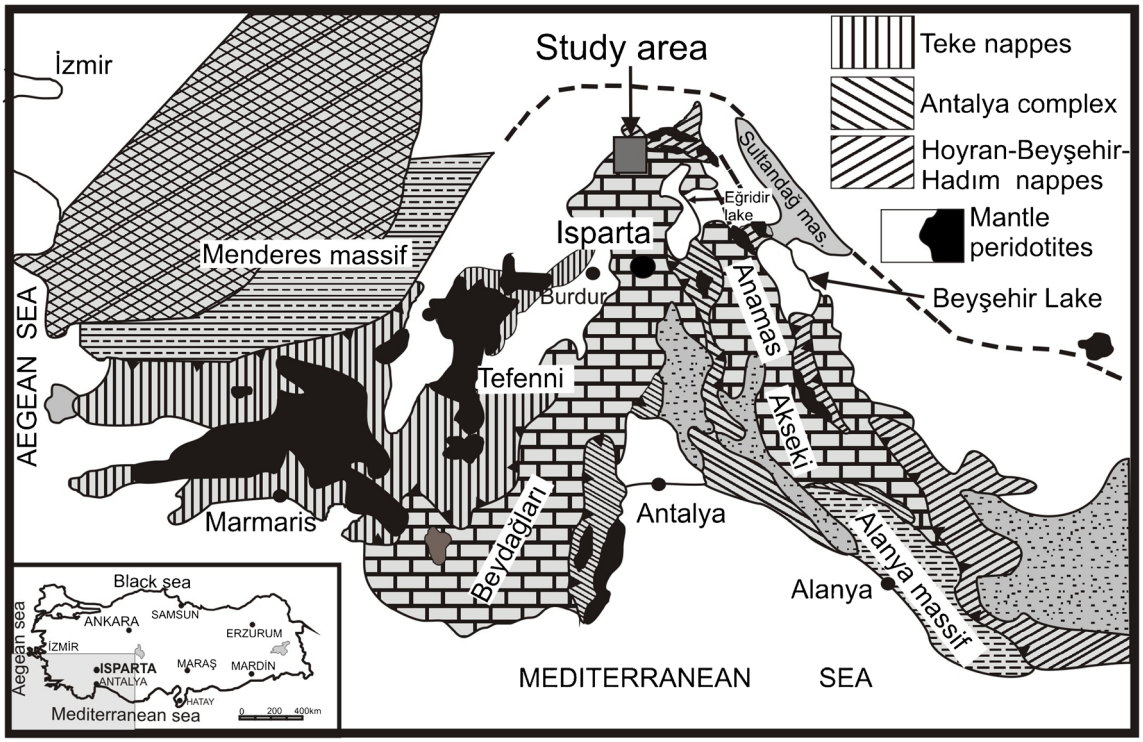

Fig. 2 Simplified geological map of the Isparta Angle area (modified from Juteau 1980)

allochthonous ophiolitic rock units; from west to east the Teke nappes (Lycian nappes), the Antalya complex and the Hoyran-Beyşehir-Hadım nappes.

Southwestern Turkey is a complex geodynamic area which has been subjected to compressional and extensional tectonic activities, ophiolite emplacements, block rotations, volcanic activities from Paleozoic to present day. North-south trending volcanic rocks crop out from the apex of the Isparta Angle (Gölcük volcano, Isparta) to the north of Afyon (Kırka area) including the study area. KAIVP is characterized mainly by potassic–ultrapotassic volcanic rocks (Alıcı et al. 1998; Francalanci et al. 2000; Platevoet et al. 2008, 2014; Elitok et al. 2010). Regional tectonic evolution of southwestern Turkey including the KAIVP is in close relationship with the main paleotectonic and neotectonic evolution of Turkey. Collision of the African and Arabian plates with the Eurasian plate along the Hellenic arc to the west and the Bitlis–Zagros Suture Zone (BZSZ) to the east has been accompanied by tectonic escape of most of the Anatolian crustal block to the west–southwest toward the Aegean–Cyprean arc system by major strike-slip faulting on the right-lateral North Anatolian Transform Fault Zone (NATFZ) and left-lateral East Anatolian Transform Fault Zone (EATFZ) since the upper Miocene (Şengör 1979; Şengör and Yılmaz 1981; Şengör et al. 1985; Dewey et al. 1986 and references therein; Dilek and Moores 1990; Tatar et al. 1996; Hubert-Ferrari et al. 2003; Allen et al. 2004; Barazangi et al. 2006; Dilek et al. 2007). The westward escape of the Anatolian plate has been accompanied by counterclockwise rotation as well as lateral translation deduced from GPS and paleomagnetic data (Tatar et al. 1996; Reilinger et al. 1997; Platzman et al. 1998; Gürer and Gürer 1999; McClusky et al. 2000; Özçep and Orbay 2000; Bozkurt 2001; Büyüksaraç 2007). Therefore, the timing of collision-induced westward extrusion of the Anatolian plate has been widely accepted as the commencement of the neotectonic history of Turkey (Şengör and Yılmaz 1981; Koçyiğit et al. 2001).

Koçyiğit (1984a, b) subdivided the tectonic development of southwestern Turkey and adjacent areas into three periods such as the Paleotectonic period (Liassic–Maastrichtian), Transition period (Upper Lutetian–Middle Oligocene), and Neotectonic period (which initiated locally at the end of Middle Oligocene, but regionally in the Late Miocene to Early Pliocene). He also interpreted that transition period is characterized by a thick pile of molasse formation and the Neotectonic period characterized by regional uplift, continental sedimentation, synsedimentary volcanism, and block faulting which was developed under the control of tensional tectonic regime. In the northern part of the Isparta Angle, Upper Miocene–Pliocene potassium-rich alkaline within plate volcanics (e.g., trachyte, leucite-trachyte, leucite aegirine trachyte, leucitite, leucite-bearing tuffs, tuffite, agglomerate) are either vertically or laterally transitional with terrestrial sedimentary units or occur as dyke or lava domes in relation with graben-forming tectonic structures, suggesting close relationship between extension-related block faulting and volcanic

activities. On the other hand, this area includes active faults producing high-intensity earthquakes reaching magnitude 8.

Geology of the study area

The study area is located at the apex of the Isparta Angle and within the KAIVP. It is bounded by east-west trending Senirkent graben in the south and northeast-southwest trending Haydarlı graben in the north (Figs. 3, 4, and 5a). Also, numerious faults in different sizes can be observed within the study area. Mesozoic formations consisting mainly of carbonate rocks form the basement rocks. They were intruded by Tertiary volcanic rocks and also overlain by Tertiary silicaclastic and volcano-sedimentary deposits. Alluvial and slope debris materials are recent deposits. Different names were used for the same formations in different studies, which causes information confusion. In this sudy, the formation names were used as given in the study of Balcı (2011).

Uluğbey Formation

Uluğbey Formation, located north of Uluğbey village, consists mainly of thin-moderate bedded, in places thick-bedded, gray-light gray dolomitic limestones, and massive limestones. Massive limestones can be observed especially at the uppermost part of the formation. Although the lower contact is not observed in the study area, its outcrop thickness reaches up to maximum 200 m. On the bases of fossil content and age of overlying units, its age was interpreted as Middle Jurassic (Balcı 2011).

Ergenli Formation

Ergenli Formation is composed of gray, dark gray, beige, bluish-gray, mainly moderate-thick bedded but in places massive limestones/dolomitic limestones. The base of the formation is not seen in the study area. However, its top is either concordant with the Gökhacıdağ Formation or overlain unconformably by the volcano-sedimentary deposits. On the other hand, the initial contact relation with the Dereköy Formation was disrupted, most probably due to ophiolite emplacement and graben-forming tectonic activities. Its age was determined as upper Jurassic (Balcı 2011).

Gökhacıdağ Formation

Gökhacıdağ Formation starts with dark gray, gray, beige, bluish-gray colored, moderate-thick bedded limestone/dolomitic limestones, in places, with thin bedded, pinkish-purple cherty micritic limestones at the base. Pinkish-purple, thin-bedded and microfolded cherty micritic limestones are observed especially in the north of Başköy village. The formation passes upward white, beige, gray, medium-thick bedded, in places massive, and highly fractured limestones/dolomitic limestones. White and beige limestones of this formation are quarried for marble production. The age of the formation was interpreted as Lower Cretaceous to Lutetian (Balcı 2011).

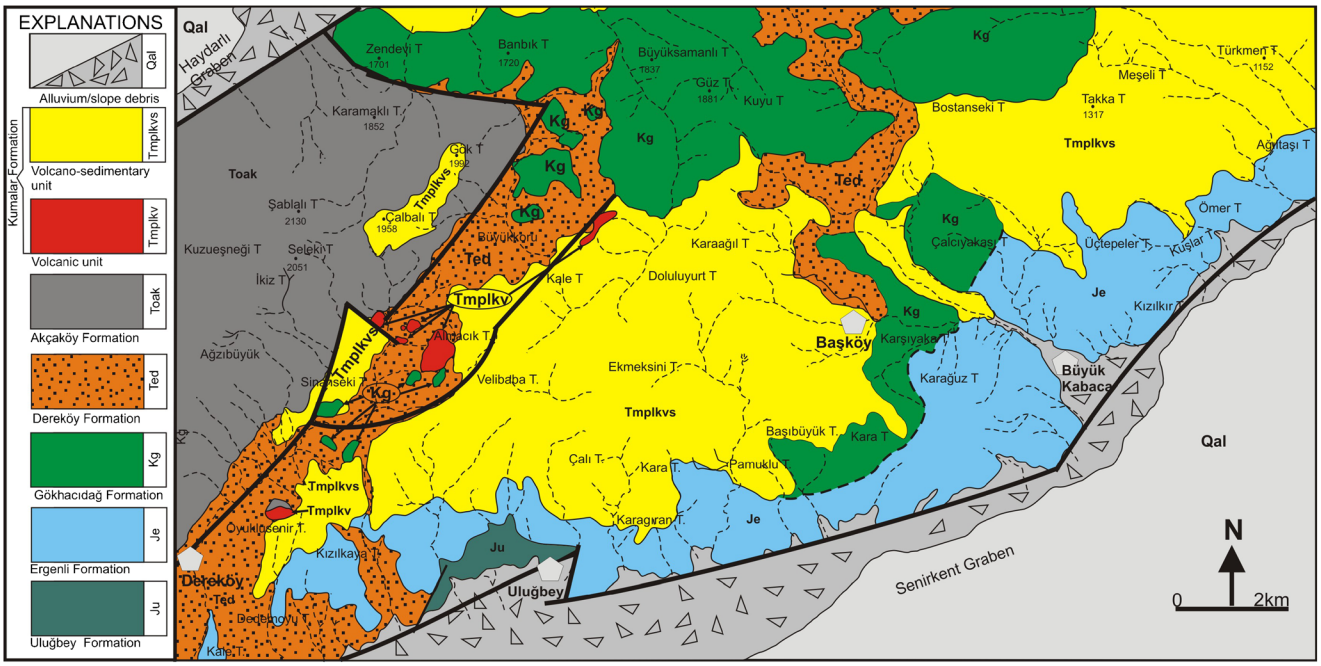

Fig. 3 Geological map of the north of Senirkent area (Isparta, southwestern Turkey)

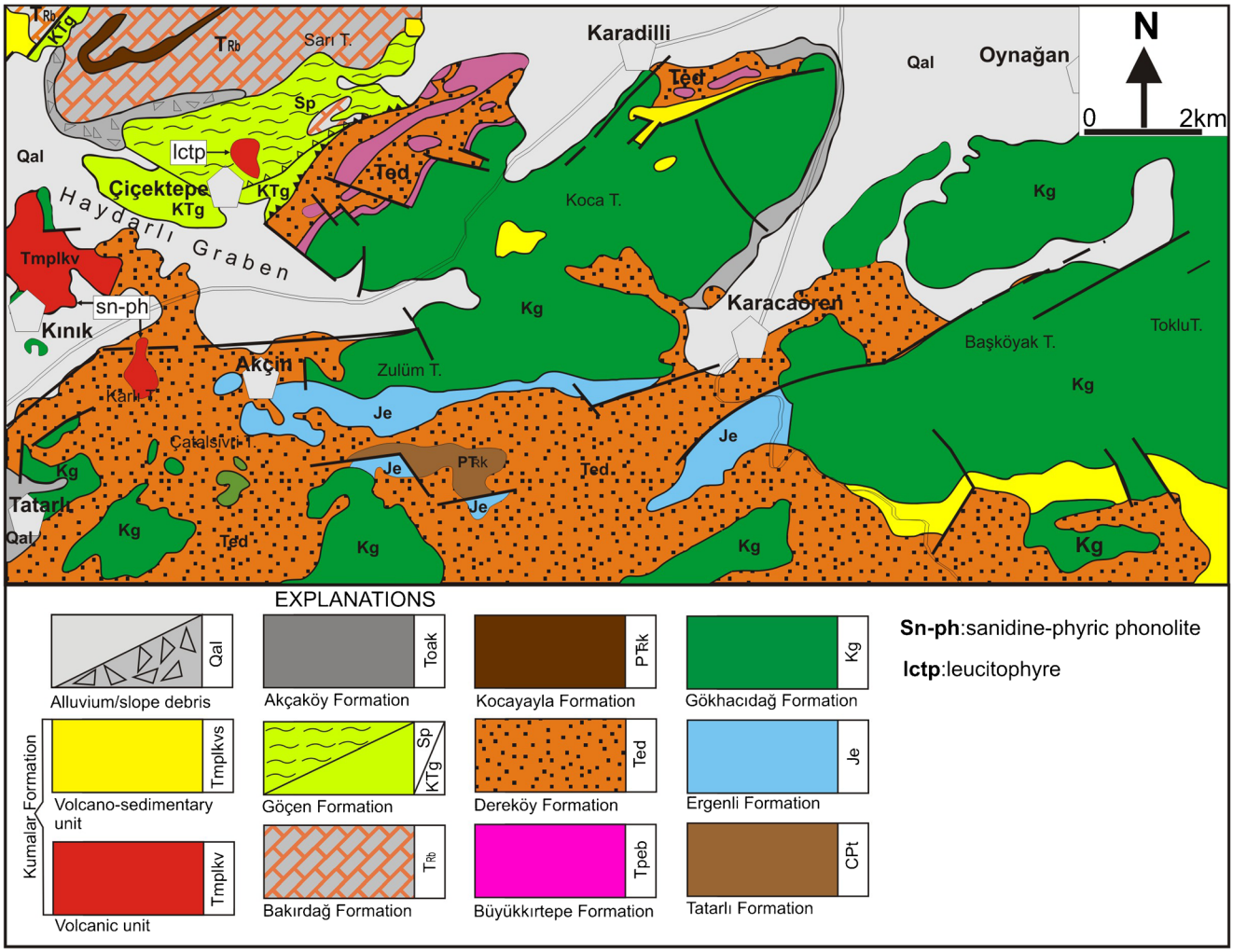

Fig. 4 Geological map of vicinity of Çiçektepe, north of Senirkent area (modified from Balcı 2011)

Dereköy Formation

Dereköy Formation consists mainly of turbiditic sandstone, clayey-sandy limestone, shale, marl, and mudstone alternations. Yellow, green, yellowish-green, light-brown, thin to thick bedded, and fine- to coarse-grained sandstones form the majority of the formation. Sandstones include mainly carbonate rock grains and ophiolitic materials. On the basis of fossil content, Koçyiğit (1984b) determined the age of the formation as Lutetian.

Akçaköy Formation

Akçaköy Formation overlies unconformably the Dereköy Formation and consists mainly of medium- to well-rounded clasts of limestone, radiolarite-chert, serpentinite, gabbro, diabase, peridotite, sandstone, brecciated conglomerate, conglomeratic limestone blocks, meter-sized limestone blocks displaying puding structure, and tuff materials. It crops out mainly around Küçükkabaca and north of Dereköy village. Koçyiğit (1984a) interpreted this formation as post-orogenic molasse and, according to fossil content, determined its age as Lower-Middle Oligocene.

Kumalar Formation

Kumalar Formation includes mainly potassic lava extrusions and volcano-sedimentary deposits derived mostly from the basement rocks and volcanic extrusions. Lava extrusions are observed as gray, dark gray, lava domes, and flows (Fig. 5b). Volcano-sedimentary deposits are composed of tuff, tuff breccia, agglomerate, sandstone, siltstone, and claystone layers in various thicknesses. Agglomerate, tuff, tuff-breccia include limestone clasts. Along the Uluğbey-Tatarlı road, tuffs are mainly fine grained, gray, yellowish-green, and rest on limestones. Limestones in this area are gray, dark gray, and in places are brecciated along the valley. Koçyiğit (1984b) interptered that brecciated limestones with thickness of 3–5 m between lower shallow carbonates and upper flysch-type deposits represent the sudden change from shallow to

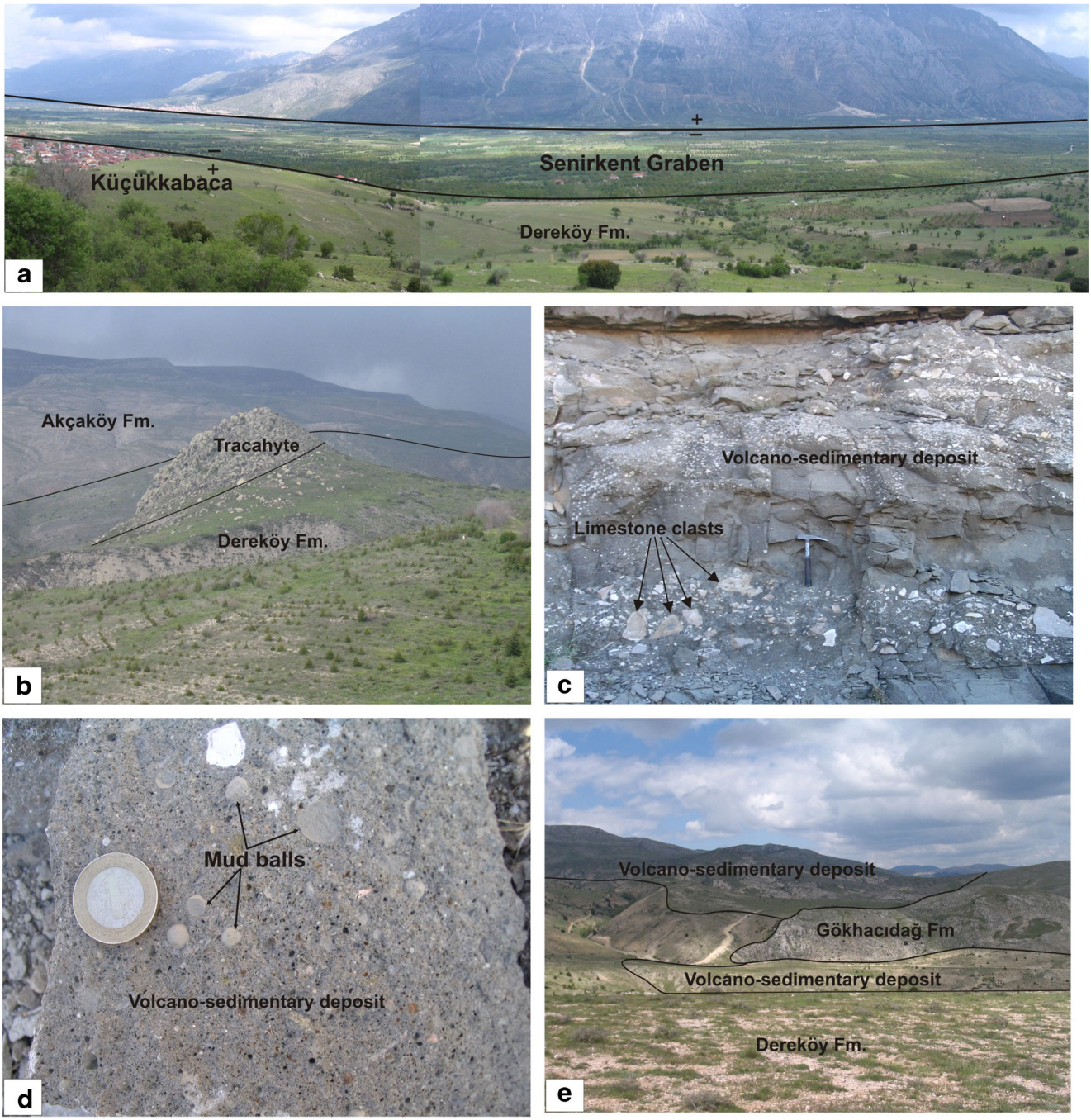

Fig. 5 Field view of **a** Senirkent graben, **b** trachytic lava dome intruding the Dereköy Formation, **c** carbonate rock fragments, **d** mud balls within the volcano-sedimentary layers, and **e** volcano-sedimentary unit (Kumalar Fm) overlying the carbonate rocks (Gökhacıdağ Fm) and turbidite deposits (Dereköy Fm)

deep sea conditions. In general, oriented angular to subrounded limestone clasts are oberved at the bottom of the tuff layers (Fig. 5c) and mafic-felsic minerals, mud balls (Fig. 5d) are observed within the tuff layers. Moreover, lenticular or birds-eye like calcite infillings are observed. Tuffs are mainly in different color (dark gray, gray, beige, pale pink), medium to thick bedded, and include locally clastics of carbonate rocks. However, thick tuff layers display millimeter- to centimeter-sized thin bedding in itself. On the basis of paleontological data (İnal 1975; Erişen 1972) and radiometric age determinations from biotite minerals within pyroclastics (Becker-Platen et al. 1977), the age of the formation can be interpreted as Upper Miocene–Pliocene. The volcano-sedimentary unit overlies unconformably the older carbonate and silicaclastic units in the study area (Fig. 5e).

Petrography

Rock samples were collected from both the lava flow domes and magmatic rock fragments of the volcano-sedimentary deposits in the study area. Within the study area and adjacent areas, outcrops of some rock types in the composition of magmatic rock fragments taken from the volcano-sedimentary deposits are not observed as extruded lava masses such as lava flows or domes, etc. Taking into consideration leucite content, potassic and ultrapotassic rocks can be classified under two subgroups; leucite-bearing rocks and leucite-free rocks. Leucite-bearing rocks are nepheline-foidolite, italite, leucitite, melilite leucitite, melilite-gehlenite leucitite, diopside leucitite, phonolitic leucitite, and leucitophyre. Leucite-free rocks are sanidine-phyric phonolite and trachytes. Leucite-bearing and leucite-free rocks include clinopyroxene but plagioclase is absent. Çoban et al. (2003) studied the mineral chemistry of pyroxene minerals in the vicinity of the study area. They interpreted that core and margin of the pyroxenes vary between diopside and hedenbergite composition. Of which, leucitophyre, phonolitic leucitite, sanidine-phyric phonolite, and trachytes occur as lava domes and limited lava flows. Other magmatic rock types are found as clastics in different sizes within the volcano-sedimentary deposits in the study area. However, outside the study area, Akal (2003) observed melilite leucitites as domes and spatially limited lava flows around Meşebaşı Tepe and Göktepe near Balçıkhisar (Afyon).

Italite

Italite is found as volcaniclastic grains in the area and mainly shows holocrystalline texture. The mineral assemblage of the italite is leucite, diopside, phlogopite, garnet (melanite), and apatite minerals (Fig. 6a). Leucite, pyroxene, and garnet minerals occur as major phases and small, prismatic apatite minerals are present as accessory mineral in the rock. Leucite minerals vary from moderate to coarse grain size, from euhedral to anhedral forms. They show mainly complex polysynthetic twinning. Especially, coarse leucite crystals include biotite needles. Leucite crystals mainly form crystalline texture together with tripple junction at the crystal boundaries. They are replaced by analcime around crystal edges or adjacent to internal cracks. Clinopyroxene minerals (diopside) are mainly in anhedral forms. They are colorless or display pale green color under plane polarized light (PPL) and first-order yellow to second-order interference colors under cross polarized light (XPL). Leucite, biotite, and garnet minerals are embedded in or can be observed as inclusions within the pyroxene minerals giving rise to skeletal form to the pyroxene minerals (Fig. 6b). Also, apatite minerals can be included within the proxene minerals. Garnet minerals (melanite) are mainly granular and in subhedral to anhedral forms. They are isotrop under XPL and show a brownish color under PPL (Fig. 6a, b). Phlogopite minerals are mainly subhedral to anhedral forms and display green and brown pleochroism under PPL. Leucite and garnet minerals are embedded in phlogopite minerals or occur as inclusions within the phlogopites. Also, phlogopites cut pyroxenes or they are embedded in the proxene minerals or occur as inclusion within the pyroxene minerals. Also, phlogopites can be observed within the pyroxene crystals as discontinous patchy forms displaying optical continuation. Pyroxenes show sieve texture as a result of remelting, and this side of pyroxenes includes phlogopites.

Leucitite

Leucitites are present as volcaniclastic grains in the field and show porphyritic texture with 70–80% phenocryst and 20–30% groundmass. The phenocryst assemblage consists mainly of leucite (nearly 60–70% of all phenocrysts and some of them analcimitized), clinopyroxene minerals, and very less (< 1%) nosean and apatite microphenocrysts. The groundmass consists mainly of microlitic feldspar displaying flow texture and finer pyroxene and opaque minerals. Leucite minerals are mainly in subhedral to andhedral forms and resorbed by groundmass along their edges (Fig. 6c). They show mainly complex twinning. They are wholly or partly replaced by secondary analcime (Fig. 6d). Small pyroxene minerals can be included within the leucite crystals. Proxenes are in euhedral to anhedral forms and display second–third-order interference colors. Some pyroxenes show optical zoning or simple twinning. Also, they can be found as inclusions within another pyroxene mineral. They are resorbed by matrix along their margins. Under PPL, they have a light greenish color, some of them colorless in the cores and greenish color on the margin. In places, pyroxenes are observed as glomerophyre aggregates. Nosean crystals are mainly in subhedral forms and display first-order interference color under XPL. They are colorless or show earthy view along their margins under PPL. Prismatic apatite minerals are found in minor amount within the rock. Some parts of the rock has different feature that carbonate globules, subangular carbonate grains, phlogopite, clinopyroxene, garnet (melanite) crystals can be observed within the mixed volcanic and carbonate matrix.

Diopside leucitite

Diopside leucitite is found as volcaniclastic grains in the area and has porphyritic texture with diopside and leucite phenocrysts (Fig. 6e). Leucites are sometimes replaced with analcime minerals. Diopside crystals display first- to second-order interference color, euhedral to anhedral forms. Lath-shaped and typical eight-sided pyroxene section to the long axis can be observed. They can show optical zoning and simple twinning. They are light green under PPL. Groundmass is

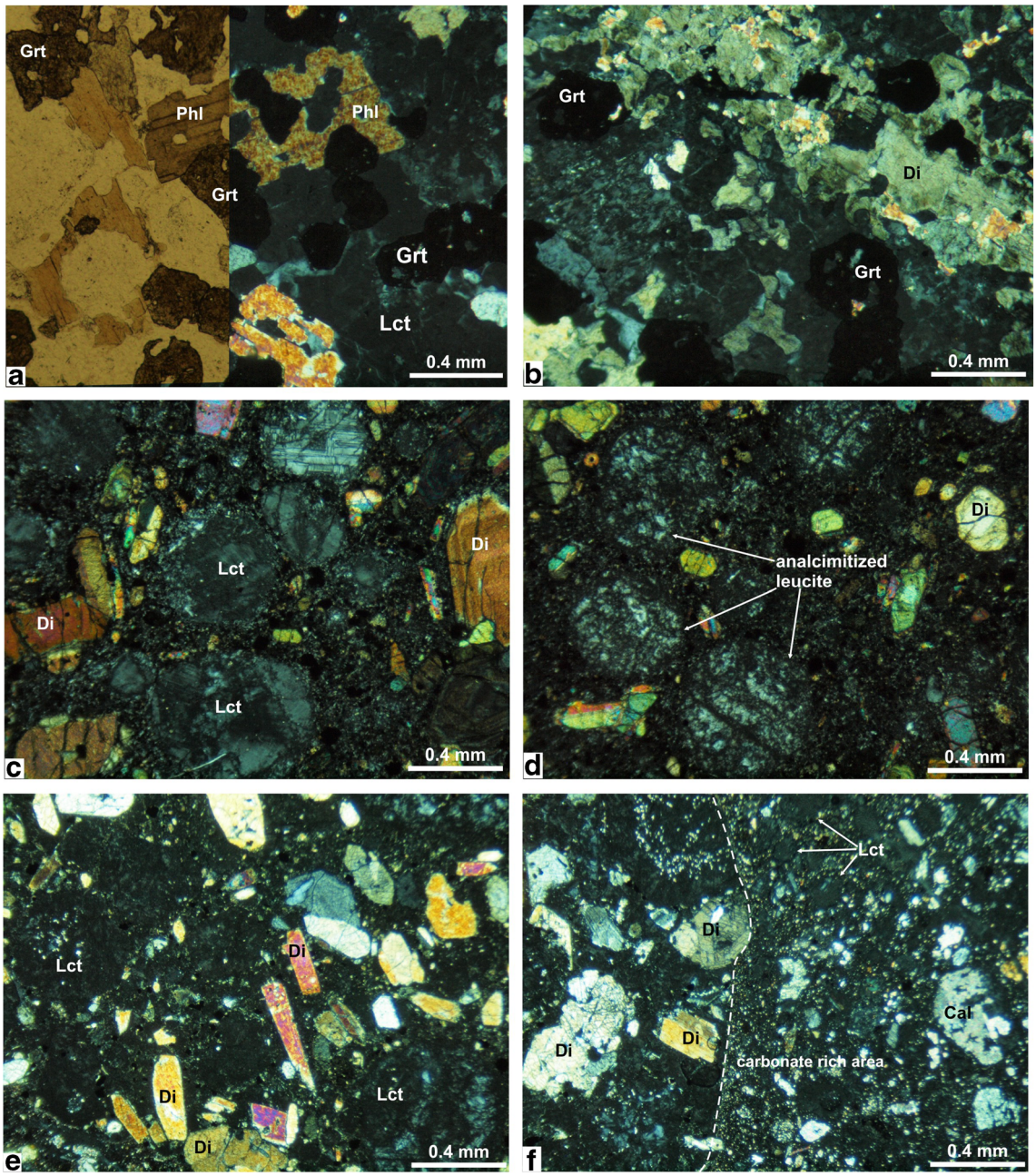

Fig. 6 Thin-section view of **a**, **b** italite, **c** subhedral to andhedral leucite, **d** analcimitized leucite, **e** diopside leucitite, and **f** carbonate-rich diopside leucitite. Lct, leucite; Grt, garnet (melanite); Phl, phlogopite; Cal, calcite

composed of volcanic glass, microlitic pyroxenes. Apatites are observed in acicular foms. Tiny euhedral to anhedral opaque minerals are found in minor amount. One side of the rock has different feature that carbonate globules, subangular carbonate grains, leucite, garnet (melanite), taeniolite (mica), and clinopyroxene crystals can be observed within the mixed volcanic and carbonate matrix (Fig. 6f). However, garnet minerals do not occur in the diopside leucitite side. Opaque minerals are fine grained and euhedral to anhedral forms.

Melilite leucitite

Melilite leucitites are present as volcaniclastic grains in the field and show porphyritic texture with 70–80% phenocryst and 20–30% groundmass. About 60–70% of the microphenocrysts are leucite crystals, and melilite is the second mineral in order of abundance. Leucite minerals are mainly round shaped resorbed along edges of crystals (Fig. 7a). Melilite minerals mainly show long lath habit and resorbed mainly along crystal edges (Fig. 7a). They are colorless under

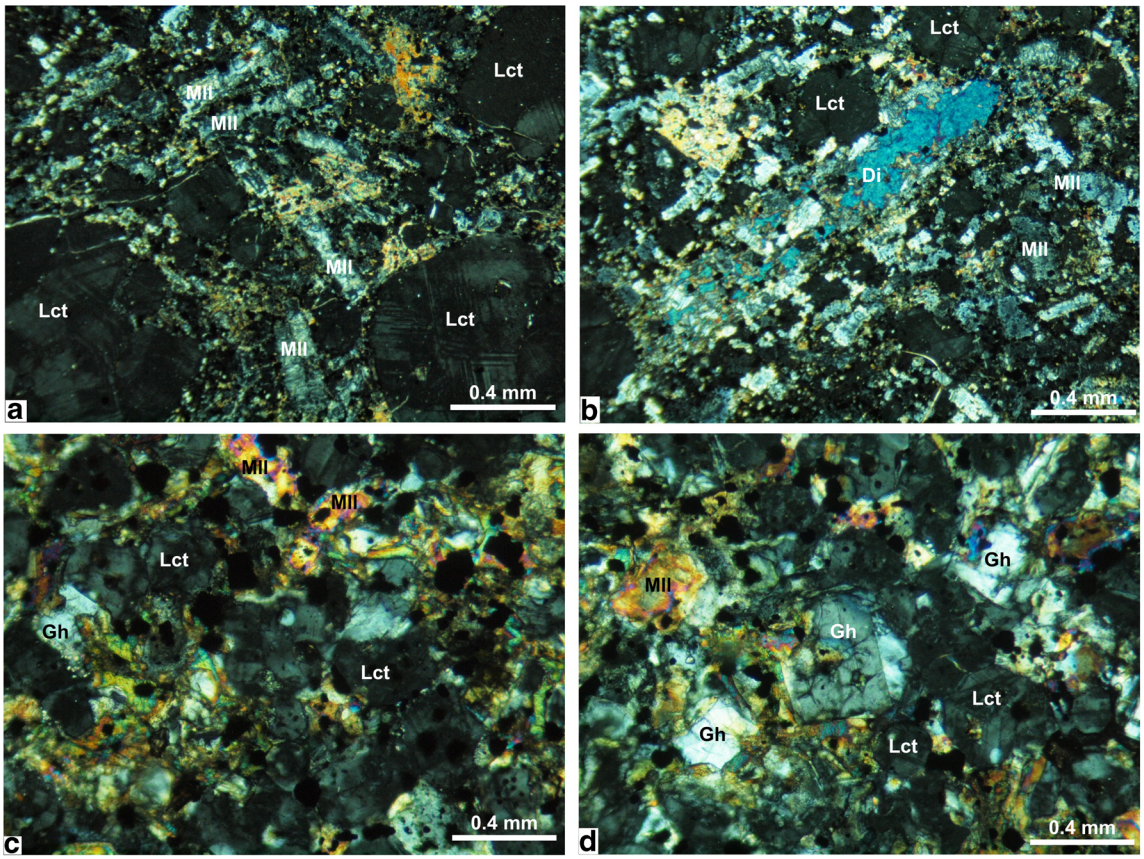

Fig. 7 Thin-section view of **a** round-shaped, resorbed leucite, **b** anhedral diopside minerals in melilite leucitite, and **c**, **d** leucite, melilite, and gehlenite minerals in melilite-gehlenite leucitite. Mll, melilite; Lct, leucite; Gh, gehlenite.

PPL and display gray and bluish-gray interference color under XPL with yellow color zone along the crystal margins. Some of them show peg structure. Apatite minerals are mainly in prismatic forms with brownish color along their margins, but also some apatites are resorbed along crystal edges. Phlogopites occupy among the minerals or often occur as intersitial phase, and they display sieve texture. Melilite minerals are often enclosed by interstitial phlogopites. Clinopyroxene (diopside) minerals are resorbed along the crystal edges and display sieve texture due to remelting. They are mainly replaced by melilite minerals (Fig. 7b). There are dispersed fine-grained opaque minerals within the ground mass. On the other hand, tiny opaque minerals are present along the pyroxene margins.

Melilite-gehlenite leucitite

Melilite-gehlenite leucitites are observed as volcaniclastic grains in the field and include leucite, diopside, gehlenite, melilite, phlogopite, and opaque minerals (Fig. 7c, d). These rocks display holocrystaline texture. Leucites are equigranular or in different sizes and mainly round-shaped with complex twinning. They constitute about 60–70% of the rock. They are isotropic under XPL and colorless under PPL. Pyroxene minerals are mainly anhedral and display first- to second-order interference color under XPL. They are colorless and/or display light green color under PPL. They are found as an interstitial mineral between the leucite and gehlenite minerals. Also, pyroxene minerals are embedded in the leucite and gehlenite minerals or they are corroded along their margins by pyoxenes. Gehlenite minerals display first-order grayish interference color under XPL and colorless under PPL. They are mainly in euhedral to anhedral forms and platy or rectangular in shape. Melilite minerals are mainly in subhedral to anhedral forms with long lath tabular habit and resorbed mainly along crystal edges. They show first-order gray to bluish-gray and pinkish-red color under XPL. Fine-grained subhedral to anhedral titanite minerals are present within the rock. Tiny opaque grains are observed within or among the minerals.

Phonolitic leucitite

Phonolitic leucitites are found as volcaniclastic grains in the study area and have porphyritic texture with 50–80% phenocrysts consisting mainly of leucite, diopside, and sanidine (Fig. 8a, b). Of which, leucite crystals constitute 80–90% of the phenocrysts, and augite with sanidine crystals make up of 10–20% of the phenocrysts, but

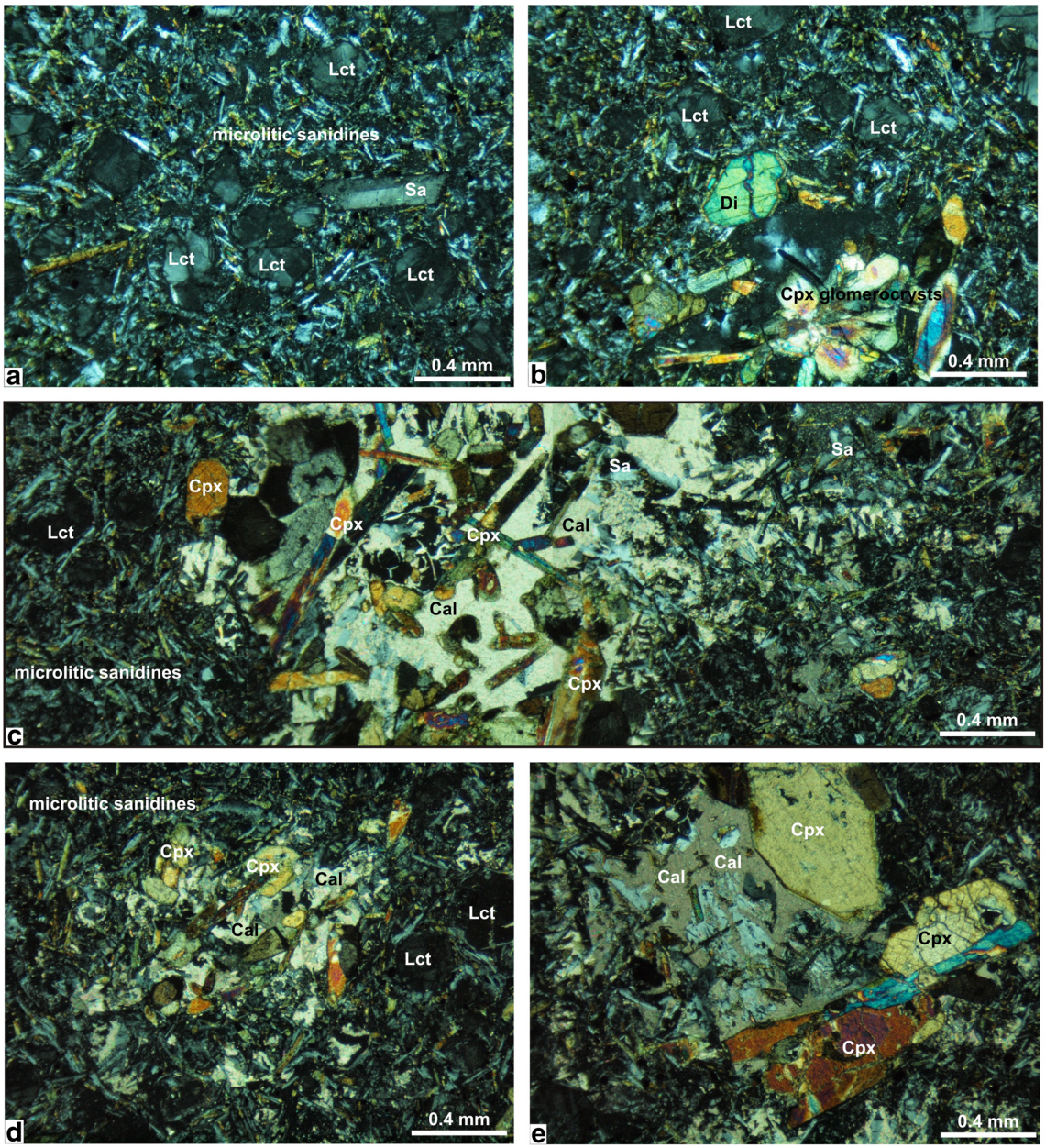

Fig. 8 Thin-section view of **a** leucite and sanidine minerals, **b** leucite and clinopyroxene glomerophyres, and **c**–**e** leucite, clinopyroxene, and carbonatite occurences within the phonolitic leucitite. Lct, leucite; Cpx, clinopyroxene (diopside); Sa, sanidine; Cal, calcite (carbonatitic).

sanidine < 5%. Leucite minerals are mainly round shaped, resorbed by matrix along crystal edges, and display complex twinning. Diopside minerals are in subhedral to anhedral forms and show optical zonning. They display mainly second-order interference color and green, light green, yellowish-green pleochroism. Some pyroxene crystals have colorless core and green-colored margin under PPL. Diopside crystals are present as single phenocrysts or glomerophyres (Fig. 8b) with or without carbonate occurences within the groundmass. Sanidine minerals exhibit simple twinning and are resorbed along crystal edges. Groundmass consists of microlitic feldspar, pyroxene, tiny granular opaque minerals, and volcanic glass. Mainly 80–90% of the microlitic phase is sanidine, and all microlitic phases display flow texture. In places, pyroxene crystals accumulate into glomerophyres and carbonate matrix (carbonatite) occupy among the glomerophyres (Fig. 8c–e). They are surrounded by calcites or occur as interlocking crystals with intricated grain boundaries. Also, pyroxene minerals are in subhedral to anhedral forms, resorbed along crystal edges by carbonate matrix. On the other hand, calcite occurences can be observed within the pyroxene minerals such as pathcy or small shapless carbonate melt inclusions. Coarser calcites

show rombohedral cleavage. Sanidine and leucite crystals can be observed within the calcite occurences. Leucites are resorbed by carbonate matrix along crystal edges and can be identified with their complex polysynthetic twinning. The boundary between the main rock and carbonate-rich side is not sharp. Sanidine minerals are distributed transitionally from leucitic main rock side to the carbonate-rich side. Opaque minerals do not occur within the carbonate-rich side. Moreover, carbonate occurences can be observed as patchy forms or infilling material within the microlitic matrix.

Mainly fine-grained carbonate-rich (carbonatitic) part of the rock include phlogopite, clinopyroxene, leucite, nosean crystals, and also carbonate globules (Fig. 9a, b). On the other hand, Fe-oxides are enriched along the margin of the carbonate-rich areas. Some phonolitic leucitites have heterogenous grain size distribution, most likely due to leucite crystals are transformed to sanidine crystals in various degrees,

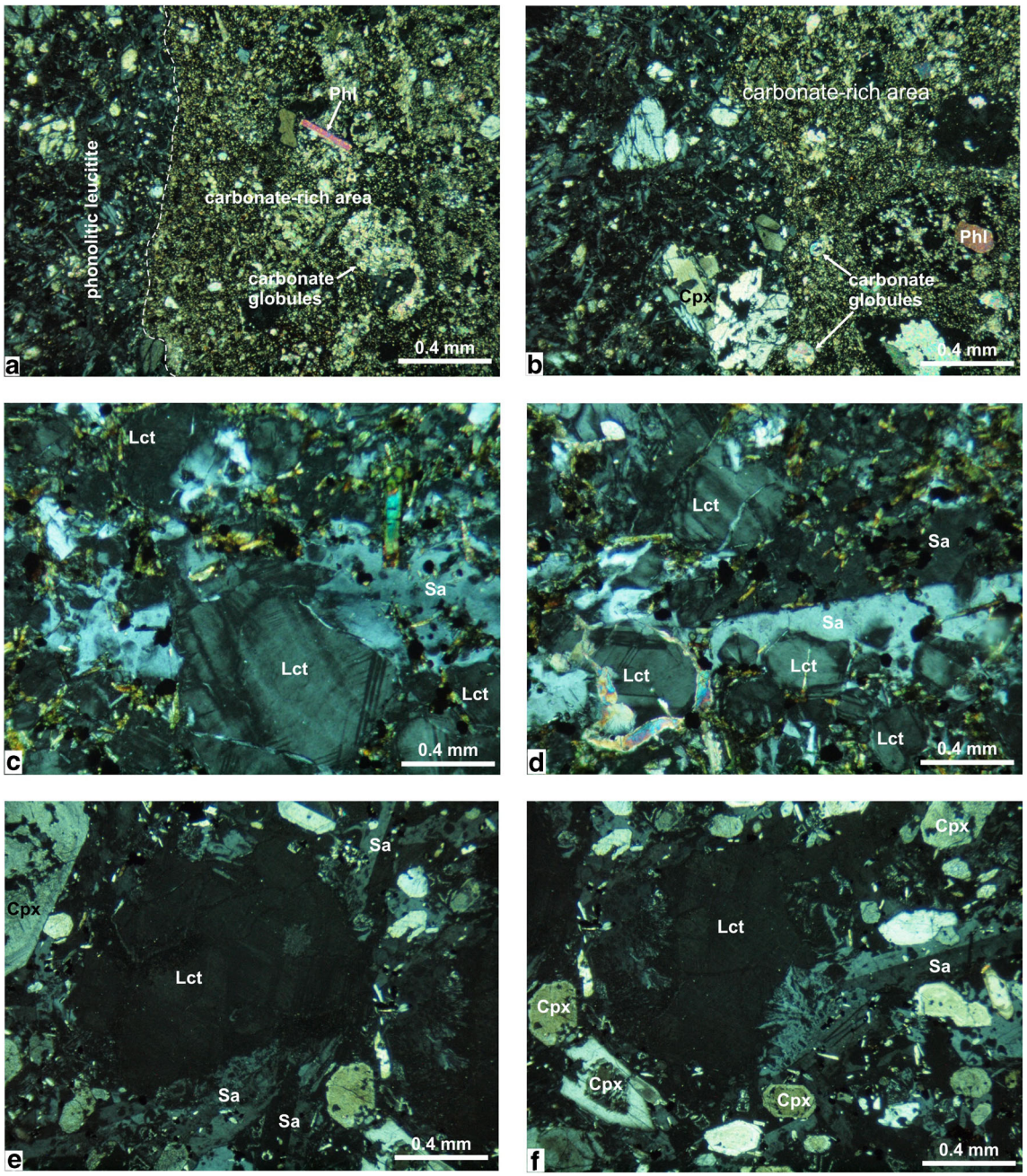

Fig. 9 Thin-section view of **a**, **b** carbonate globules within the phonolitic leucitite, **c**, **d** leucite crystals within the phonolitic leucitite, and **e**, **f** leucite phenocrysts within leucitophyre that transformed to sanidine crystals in various degrees forming corse-grained sanidine crystals with simple twinning. Lct, leucite; Phl, phlogopite; Sa, sanidine

forming coarse-grained sanidine crystals with simple twinning (Fig. 9c, d).

Leucitophyre

Leucitophyre has holocrystalline porphyritic texture with large leucite phenocrysts and crystalline groundmass including small- to moderate-sized sanidine, clinopyroxene crystals and smalll opaque, apatite minerals in minor amount. In leucitophyres, similar to phonolitic leucitites, leucite phenocrysts are transformed to sanidine crystals in various degrees, forming corse-grained sanidine crystals with mainly simple twinning (Fig. 9e, f). Leucite phenocrysts are mainly anhedral and uneven contact relation with the neighboring crystals, especially with sanidine crystals. They have cross-hatched twinning. The contact of sanidines with leucite phenocrysts are in places symplectit (Figs. 9f and 10a). Sanidine minerals display mainly simple twinning, and they enclose opaque and clinopyroxene microcrysts, or pyroxene minerals are partly embedded in the sanidines (Fig. 10b). Clinopyroxenes are in subhedral to anhedral forms and in diopside composition (Çoban et al. 2003). They display yellowish-green color or some of them have green core and colorless to light yellow green margin under PPL. Some pyroxene minerals have trace of remelting in the core. Tiny opaque minerals and acicular pyroxenes can be observed within both microlitic matrix phase and coarse-grained sanidines which were derived from the transformation of leucites. Patchy carbonate occurences can be observed within these rocks.

Sanidine-phyric phonolite

Sanidine-phyric phonolites are observed as limited lava flows around Çiçektepe and show porphyritic texture with 60–70% of sanidine phenocrysts and 30–40% groundmass. Grain size of sanidine phenocrysts can reach up to a few centimeters in hand specimens. Groundmass is made up of microlitic and microcrystal sanidine, diopside and tiny opaque minerals. Phenocrysts are mainly sanidine, but minor nosean and diopside minerals can be observed. Sanidine phenocrysts display mainly well-developed simple twinning and some crystals are resorbed along their edges by groundmass (Fig. 10c). Diopside crystals have subhedral to anhedral forms, and some of them display simple twinning or optical zonning. They display mainly second-order interference color under XPL and green, light green, yellowish color under PPL. Some pyroxene crystals have colorless core and green colored margin under PPL. Nosean minerals are mainly fine- to moderate-grained and in subhedral to anhedral forms. They are isotropic under XPL and colorless to yellow, yellowish-brown with earthy view under PPL. Sphene crystals can be observed in euhedral to subhedral forms with lozenge-shaped crystal forms. Apatite minerals are mainly small prismatic or hexagonal forms.

Trachyte

Trachytes display porphyritic texture with abundant sanidine phenocrysts, clinopyroxene, titanite, opaque minerals (Fig. 10d). Sanidine minerals make up nearly 90–95% of the phenocrystal phase. They are mainly in euhedral to anhedral forms, and anhedral ones are resorbed along their edges by groundmass. They mainly exhibit simple twinning. In some trachytes, sanidines display heterogenous crystal size distribution varying from microlite to phenocrystal sizes in the same rock. Pyroxene minerals are observed as subhedral to anhedral forms in lath-shaped or eight-sided crystal forms. They are also found as phenocrysts and groundmass material. Microlitic pyroxene minerals can be enclosed by sanidine minerals. Groundmass is made up of mainly microlites and crystallites of sanidine, minor amount augite, and volcanic glass. Fe oxide, opaque minerals, most likely magnetite minerals, are observed both as coarse-grained euhedral crystals and fine-grained minerals within the matrix. Rare small titanite crystals can be observed. Phenocrysts and microlitic phases display flow structure.

Carbonatite

Carbonatite consists of calcite minerals (more than 50 modal %), phlogopite, garnet (melanite), clinopyroxene, nepheline, apatite minerals (Fig. 10e, f). Clinopyroxene, nepheline, and apatite minerals are present in minor amount. Calcites are observed as interstitial phases and have, in places, well developed rhombohedral cleavages. Phlogopite and pyroxene minerals are resorbed by interstitial calcites, and also calcites are enclosed within the phlogopites. Phlogopites are medium to coarse grained and in subhedral to euhedral forms. They show yellowish-green pleochroism and second-order interference color. Some grains have rogged edges due to resorption. On the other hand, some phlogopites are embedded in the pyroxene minerals. Phlogopites can be found as glomerocrysts with crystalline texture. Garnets (melanite) are mainly medium- to coarse-grained in anhedral forms and can enclose phlogopite, calcite, and opaque minerals. They show optical zonning from dark yellow brown, dark brown in the cores to yellow, yellowish-brown, and light brown on the margins. Nepheline minerals are mainly in anhedral forms with interstitial calcite embayments. Nepheline with calcites can be found as an interstitial phase among the phlogopites. Thin and long apatite crystals are observed within the nepheline minerals or interstitial calcites. They are embedded in the phlogopites or cut by phlogopite growths.

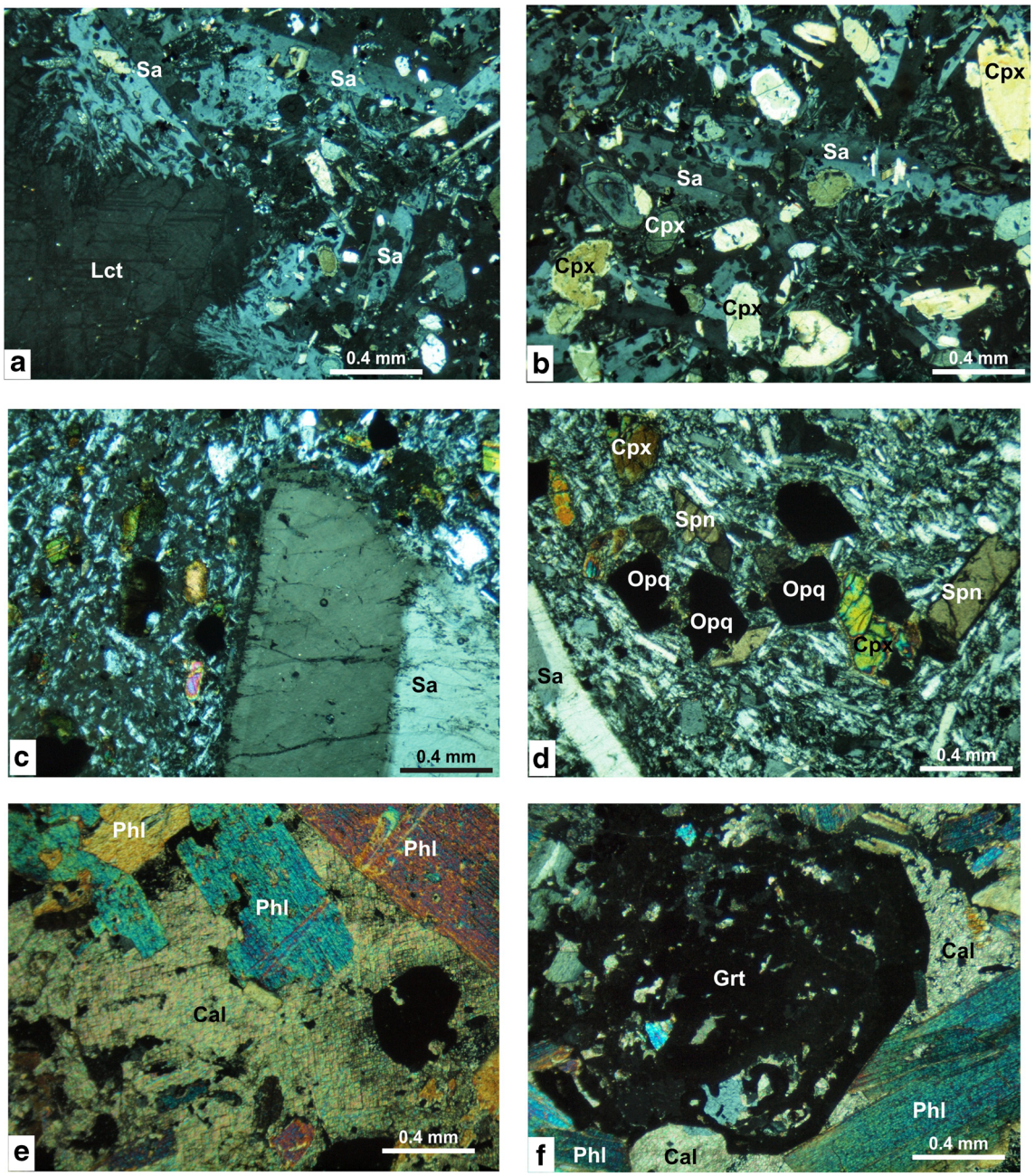

Fig. 10 Thin-section view of **a** symplectit structure developed between leucite phenocrysts and sanidine minerals, **b** clinopyroxene crystals embedded in sanidines within the leucitophyre, **c** resorbed sanidine phenocrysts in sanidine-phyric phonolite, **d** sanidine, clinopyroxene, titanite, and opaque minerals in trachyte, **e** subhedral to anhedral phlogopite minerals and coarse calcite minerals showing rhombohedral cleavage, and **f** garnet (melanite) minerals enclosing phlogopite and calcite minerals in carbonatite. Lct, leucite; Phl, phlogopite; Sa, sanidine; Grt, garnet (melanite); Cpx, clinopyroxene; Spn, sphene; Opq, opaque; Cal, calcite

Geochemistry

Major, minor and trace element analyses were carried out for 17 selected rock samples at ACME Analytical Laboratories Ltd., Canada. Loss on ignition (LOI) was determined after ignition at 1000 °C. The major and some trace elements were analyzed by ICP-AES, while some trace and rare earth elements were analyzed by ICP-MS following a lithium metaborate/tetraborate fusion and dilute nitric digestion. Average detection limit was 0.01 wt% for major oxides and in the range of 0.1–0.5 ppm for trace elements and 0.007–0.012 ppm for REE. Major oxide and trace element composition of the analyzed samples are reported in Table 1. The LOI of the 16 samples vary between 0.8 and 8.7 wt% and carbonatite sample has the highest value with 13.2 wt%. Trachytes have lower LOI values. Due to relatively high

Table 1 Representative major and trace element contents of magmatic rocks from the study area

	Ultrapotassic							Potassic									
	Sample no.																
	US-15-a ne-fd m-fr	US-12 it m-fr	US-2 lct m-fr	US-2-A ml-lct m-fr	US-15-C ml-gl-lct m-fr	US-14-1 dp-lct m-fr	HC-1 lctp l-f	US-17 ph-l l-f	US-18 ph-l l-f	US-24 ph-l l-f	US-25 ph-l l-f	SC-1 sn-ph l-f	US-20 tr l-f	US-21 tr l-f	US-22 tr l-f	US-23 tr l-f	US-13 cbt m-fr
SiO_2 (wt%)	38.71	42.86	42.02	42.39	44.43	44.72	51.4	51.77	50.78	49.35	49.55	55.79	60.60	63.91	64.05	64.46	27.42
Al_2O_3	12.81	13.82	13.5	13.15	14.68	9.88	17.2	18.94	18.46	18.58	18.73	17.71	16.77	16.97	17.17	17.05	6.92
Fe_2O_3	12.70	9.09	11.58	11.23	9.65	7.98	6.8	5.36	5.01	5.57	5.54	4.15	3.02	3.02	3.14	2.94	11.34
MgO	3.99	4.37	4.15	4.09	3.36	6.98	3.25	0.9	1.39	0.79	1.06	1.13	0.47	0.29	0.17	0.21	8.79
CaO	13.88	11.57	8.2	9.29	8.82	12.63	5.93	3.77	5.15	5.7	5.41	4.38	2.51	1.63	1.22	1.38	24.17
Na_2O	0.21	0.82	1.83	2.51	1.37	0.86	1.51	0.86	3.31	2.51	1.99	1.53	3.25	3.75	3.67	3.76	0.07
K_2O	6.89	9.82	7.3	6.64	10.19	4.36	9.6	10.16	10.67	11.32	11.38	10.54	8.28	8.42	8.5	8.46	4.26
TiO_2	2.53	1.67	1.85	1.82	1.5	1.21	1.31	0.76	0.74	0.82	0.83	0.52	0.38	0.4	0.4	0.38	1.1
P_2O_5	0.64	082	1	1	0.53	1.23	0.59	0.16	0.15	0.13	0.13	0.18	0.06	0.07	0.05	0.05	1.15
MnO	0.16	0.13	0.2	0.2	0.17	0.13	0.1	0.1	0.11	0.11	0.11	0.08	0.07	0.04	0.04	0.06	0.21
$Cr2O_3$	< 0.002	0.005	0.003	< 0.002	< 0.002	0.006	–	< 0.002	< 0.002	< 0.002	< 0.002	< 0.002	< 0.002	< 0.002	< 0.002	< 0.002	< 0.002
LOI	6.2	4.1	7.1	6.4	4.3	8.7	1.6	6.2	3.2	3.9	4.2	3.3	4.1	1	1.1	0.8	13.2
SUM	98.73	99.06	98.75	98.71	98.94	98.65	99.9	98.98	98.95	98.81	98.96	99.28	99.48	99.5	99.5	99.5	98.61
Ba	5512	3612	6374	6438	4334	6101	4324	5077	5082	5321	5234	2457	2081	1826	2104	1924	5606
Ni	4.5	13.1	15.8	14.2	5.4	5.5	37	0.5	1.2	0.5	0.2	5.9	2.1	1.2	0.6	0.6	3.7
Sc	14	12	15	15	10	16	–	2	2	2	2	4	3	3	3	3	5
Co	26	24.4	33.5	33.8	26.9	24.8	13.6	6.1	6.1	7.9	8.5	6.5	1.9	1.9	2.1	1.7	13.4
Cs	11.2	16.8	178.4	248.5	37.1	7.7	–	38.1	19.3	19.7	17.8	12.3	13.4	8.7	8.3	11.2	5.5
Ga	16.4	18	18.6	18.2	18.1	13.4	21.2	20.2	21.1	19.2	17.9	19.7	17.8	17.6	18.3	18	22.4
Hf	47.8	22.2	20.2	21.1	18.8	16.6	15.2	13.9	14.7	15.5	14.5	22.2	15.2	16	16.6	15.7	8.1
Nb	47.7	27.3	37.9	41.1	37.1	41	28.6	38.6	37.7	36.6	36.5	37.9	29.5	28.6	29.7	29.3	206.4
Rb	249	426.3	709.2	831.3	439.4	232.6	655	947.8	369.7	469.1	400.2	392.2	227.7	274.9	263.5	263.1	155.5
Sn	17	7	8	9	8	8	–	5	5	4	4	4	5	5	5	4	7
Sr	1282	1892	1558	1812	2194	2901	1583	2146	2354	3509	2245	1792	1376	1336	1292	1334	2366
Ta	4.2	1.9	2.5	2.5	2.3	2.4	1.4	2.7	2.6	2.3	2.2	1.5	1.8	2.1	1.9	1.8	4.5
Th	65.6	36.3	43.6	43.8	51.8	61.1	39.9	72.3	71.1	63.7	63.9	76.5	51.4	50.9	52.2	56.8	113
U	17.1	9.7	16.4	16.6	15.7	7.4	10.7	6.7	28.6	19.8	28.5	11	12.7	11.9	14.5	11.8	36.3
V	494	274	334	306	319	182	128	108	122	149	157	96	41	45	42	41	757
W	< 0.5	< 0.5	< 0.5	< 0.5	< 0.5	< 0.5	–	2.5	4.1	1.7	1.2	0.5	1.5	0.7	0.9	0.6	< 0.5
Zr	1714	754	733.6	773.7	666	592.7	493	575.3	559.7	562.5	566.3	807.3	540.1	543.6	541.6	532.5	586.3
Y	50.2	29.2	301	32.4	31.3	27.2	23	30.4	28.1	23.1	22.7	18	21.6	25.7	27	23.3	33.3
Mo	0.2	0.2	0.2	0.2	0.3	0.4	–	0.4	7	2.1	2.1	0.3	0.5	0.6	1.6	0.7	0.2
Cu	219	165.4	178.2	163.4	172.7	74.9	–	10.3	19	19.4	20.2	35.3	7.1	11	8.1	6.9	12.5
Pb	60.7	85.7	92.3	102.6	95.2	83.4	58	48.5	102.8	108.5	108	99.2	13.7	116.7	14.1	17.3	64.5
Zn	38	56	95	92	85	52	–	25	47	42	40	57	19	65	37	54	100
As	1.7	3.6	2.5	3.5	2.2	2.6	–	5.9	14.3	4.3	4.6	5.5	0.8	3.1	5.6	2.8	10.2
Cd	< 0.1	0.1	< 0.1	< 0.1	< 0.1	< 0.1	–	< 0.1	0.2	< 0.1	0.1	< 0.1	0.1	< 0.1	0.1	< 0.1	0.1

Table 1 (continued)

	Ultrapotassic							Potassic									
	Sample no.																
	US-15-a ne-fd m-fr	US-12 it m-fr	US-2 lct m-fr	US-2-A ml-lct m-fr	US-15-C ml-gl-lct m-fr	US-14-1 dp-lct m-fr	HC-1 lctp l-f	US-17 ph-l l-f	US-18 ph-l l-f	US-24 ph-l l-f	US-25 ph-l l-f	SC-1 sn-ph l-f	US-20 tr l-f	US-21 tr l-f	US-22 tr l-f	US-23 tr l-f	US-13 cbt m-fr
Sb	< 0.1	< 0.1	< 0.1	< 0.1	0.1	< 0.1	–	0.2	0.4	0.3	0.2	0.7	0.1	0.3	0.6	0.2	< 0.1
Ag	< 0.1	0.2	0.3	0.3	0.2	0.2	–	< 0.1	0.1	< 0.1	< 0.1	< 0.1	< 0.1	< 0.1	< 0.1	< 0.1	< 0.1
Au (ppb)	0.5	8.1	17.1	10.3	5.9	3.7	–	< 0.5	0.9	0.7	< 0.5	< 0.5	< 0.5	1.9	1.4	2.8	5.6
Hg	< 0.01	< 0.01	< 0.01	< 0.01	< 0.01	< 0.01	–	< 0.01	< 0.01	< 0.01	< 0.01	< 0.01	< 0.01	< 0.01	< 0.01	< 0.01	< 0.01
TI	1.2	2.6	11.9	10.3	1.6	1.5	–	1.9	2.1	1.6	1.7	1.4	0.4	0.1	< 0.1	< 0.1	0.5
Se	< 0.5	< 0.5	< 0.5	0.7	< 0.5	< 0.5	–	< 0.5	< 0.5	< 0.5	< 0.5	< 0.5	< 0.5	< 0.5	< 0.5	< 0.5	< 0.5
La	115.9	94.1	89.3	94.9	107.7	95.2	91.8	108	101.3	81.9	80.4	116.8	60.3	69.4	68.2	59.5	136
Ce	253.3	189.1	192.2	199.2	215.2	194.9	178	200.2	195.7	150.8	151.5	203.5	114.2	126.5	119.8	111.1	307.4
Pr	29.32	21.82	22.31	23.3	24.04	22.26	19.6	21.84	20.95	15.4	15.53	18.92	12.14	13.09	13.47	12.1	34.42
Nd	112.8	85.3	90.3	92.9	95.7	90.3	73.8	82.1	79.1	56.4	59.9	61.1	43.6	49	50.4	45.6	126.1
Sm	17.88	14.16	15.53	15.78	15.04	14.93	13.6	12.51	11.93	9.12	8.85	8.31	7.17	7.68	8.09	7.32	16.66
Eu	4.58	3.5	3.73	3.93	3.92	3.43	2.79	2.98	2.83	2.23	2.17	2.01	1.78	1.8	1.93	1.7	4.04
Gd	14.65	11.2	12.21	12.94	12.06	11.43	11.8	9.87	9.32	7.43	7.05	4.77	5.87	6.37	6.83	5.9	12.62
Tb	1.89	1.28	1.44	1.5	1.39	1.29	1.16	1.14	1.11	0.89	0.89	0.7	0.78	0.85	0.9	0.77	1.32
Dy	9.33	5.63	6.35	6.92	6.23	5.72	4.88	5.39	5.5	4.2	4.45	3.12	3.65	4.23	4.6	4	6.07
Ho	1.64	1	1.02	1.07	1.02	0.91	0.87	0.97	0.92	0.83	0.79	0.56	0.7	0.81	0.92	0.77	0.96
Er	4.51	2.44	2.7	2.93	3.03	2.29	2.29	2.94	2.75	2.37	2.21	1.59	2	2.53	2.82	2.23	2.49
Tm	0.67	0.33	0.37	0.39	0.41	0.33	0.33	0.44	0.41	0.38	0.36	0.23	0.32	0.37	0.43	0.35	0.38
Yb	4.55	2.1	2.38	2.54	2.52	2.04	2.01	2.86	2.69	2.23	2.28	1.63	2.2	2.54	2.92	2.35	2.43
Lu	0.67	0.31	0.34	0.36	0.38	0.28	0.29	0.39	0.38	0.34	0.34	0.24	0.32	0.41	0.44	0.35	0.35
$(La/Yb)_n$	18.27	32.11	26.91	26.8	30.66	33.47	32.76	27.09	27.01	26.34	25.29	51.4	19.66	19.6	16.75	18.16	40.15
$(La)_n$	489	397	377	400	454	402	387	456	427	346	399	493	254	293	288	251	574
$(Yb)_n$	27	13	14	15	15	12	12	17	16	13	13	10	13	15	17	14	14
Eu/Eu*	0.84	0.82	0.8	0.82	0.86	0.77	0.66	0.79	0.79	0.80	0.81	0.89	0.81	0.76	0.77	0.77	0.82
K_2O/Na_2O	32.8	11.5	3.99	2.65	7.44	5	6.36	11.8	3.22	4.5	5.72	6.8	2.55	2.25	2.32	2.25	60.86

ne-fd, nepheline foidolite; *it*, italite; *lct*, leucitite; *ml-lct*, melilite leucitite; *dp-lct*, diopside leucitite; *lctp*, leucitophyre; *ph-l*, phonolitic leucitite; *sn-ph*, sanidine-phyric phonolite; *tr*, trachyte; *cbt*, carbonatite; *m-fr*, magmatic fragment; *l-f*, lava flow

LOI values of some samples, all major elements have been recalculated to 100% on the water-free bases for plots on classification and variation diagrams.

Magmatic rocks of the study area can be classified as potassic and ultrapotassic, on the basis of chemical parameters suggested by Foley et al. (1987). Ultrapotassic rocks are nepheline-foidolite, italite, leucitite, melilite leucitite, melilite-gehlenite leucitite, diopside leucitite, and leucitophyre with the lowest SiO_2 content (38.71–44.72 wt%, but the leucitophyre has 51.4 wt%), higher K_2O (4.36–10.19 wt%), MgO (3.25–6.98 wt%), and K_2O/Na_2O ratio (2.65–32.8). Potassic rocks are phonolitic leucitites, sanidine-phyric phonolite and trachytes with K_2O (8.28–11.38 wt%), MgO (0.17–1.39 wt%), and K_2O/Na_2O ratio (2.25–11.8) (Table 1). Hereafter, phonolitic rocks will be used for phonolitic leucitites and sanidine-phyric phonolite. On the total alkali-silica diagram, ultrapotassic rocks and also some phonolitic leucitites plot within the foidite area and display positive trend with increasing SiO_2. However, some phonolitic leucitites, leucitophyre, sanidine-phyric phonolite passes to phonolite and tephriphonolite area (Fig. 11). Trachytes plot within the trachyte area as a separate group. However, diopside leucitite occurs within the trachybasalt area.

Potassic and ultrapotassic rocks form mainly three distinct groups on the SiO_2 vs. oxide variation diagrams (Fig. 12): group (1) nepheline-foidolite + italite + leucitite + melilite leucitite + melilite-gehlenite leucitite ± diopside leucitite, group (2) phonolitic leucitites + sanidine-phyric phonolite ± leucitophyre, and group (3) trachytes. Although they display three distinct groups, they show negative correlation for MgO, Fe_2O_3, CaO, and TiO_2 with increasing SiO_2, suggesting fractional crystallization. On the K_2O vs. SiO_2 correlation diagram, ultrapotassic and phonolitic rocks display slight increase and decrease, respectively, with increasing SiO_2. Trachytes are present as a distinct group on this diagram. All the rock types do not show any regular distribution on the Na_2O vs. SiO_2 diagram. Phonolitic rocks display slight positive correlation for P_2O_5, negative correlation for CaO and K_2O, and nearly horizontal distribution for MgO, Fe_2O_3, Al_2O_3, and TiO_2 with increasing SiO_2 content.

Ultrapotassic, phonolitic rocks, and trachytes have Ba content (3612–6438; 2457–5321; 1826–2104 ppm), Sr (1282–2901; 1792–3509; 1292–1376 ppm), and Rb (232.6–831.3; 369.7–947.8; 227.7–274.9 ppm), respectively. Multi-element patterns shed light on petrogenetic histories, including the mineralogical and chemical compositions of the source materials, partial melting, fractional crystallization and contamination, and/or mixing histories. Fluid-mobile elements such as some large ion lithophile elements (LILEs) (e.g., Cs, Rb, K, Ba, and U) and Sr concentrations are more susceptible to modification by late stage hydrothermal alteration, low-grade metamorphism, and intra-mantle mobilization by a water-enriched fluid than high field strength elements (HFSEs) (e.g., Nb, Ta, Ti, Hf, and Zr). High LILE/HFSE ratio is considered to be a characteristic feature of the subduction-related tectonic setting (Pearce and Cann 1973; Pearce and Norry 1979; Saunders et al. 1980; Pearce 1982, 1983; Shervais 1982; Pearce and Peate 1995). Patterns of incompatible elements, normalized to the primitive mantle composition of Sun and McDonough (1989), for the studied leucite-bearing and leucite-free magmatic rocks show subduction-related lavas or orogenic settings, with high LILE/HFSE ratio (e.g., strong

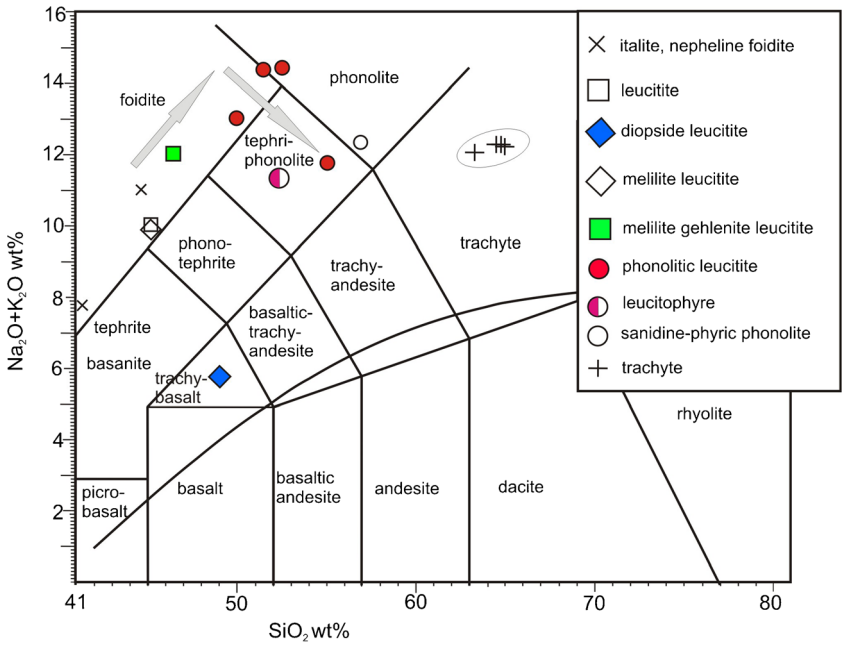

Fig. 11 Total alkali vs. SiO_2 diagram for the magmatic rocks from the study area. Classification scheme is from Le Bas et al. (1986). All the major element data have been recalculated to 100% on a water-free basis

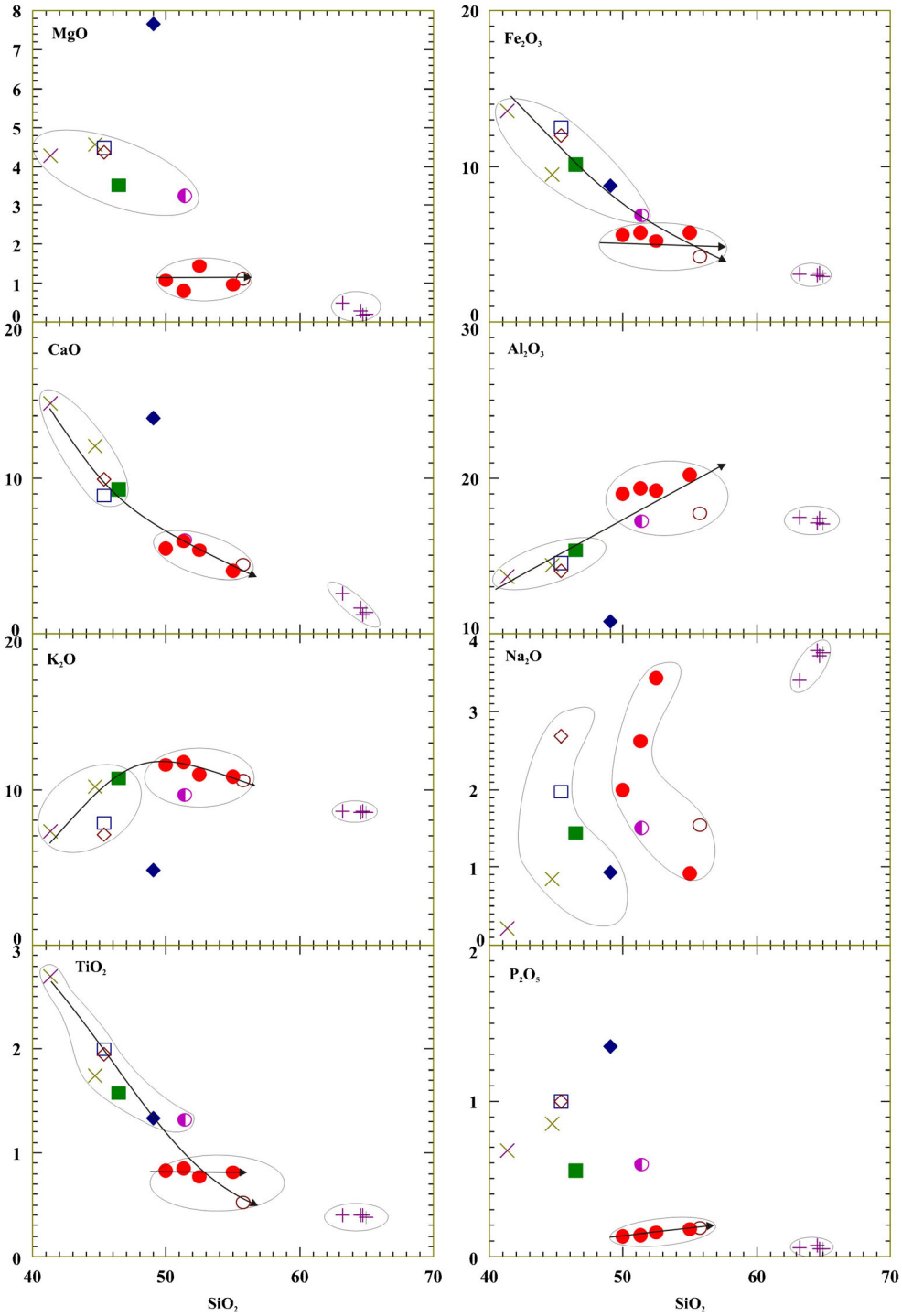

Fig. 12 Harker diagrams for some major and minor elements of potassic and ultrapotassic rocks from the study area (symbols as in Fig. 11)

enrichment in some LILEs such as Cs, Rb, Ba, U, Th, Sr relative to HFSE such as Nb, and Ti) (Fig. 13a).

Carbonatite has low SiO_2 (27.42 wt%), Al_2O_3 (6.92 wt%), Na_2O (0.07 wt%), and K_2O (4.26) but high CaO (24.17 wt%) and MgO (8.79 wt%). It displays similar pattern to the potassic and ultrapotassic rocks on the primordial mantle-normalized spider diagram and chondrite-normalized REE pattern. All the leucite-bearing and leucite-free magmatic rocks have similar chondrite-normalized REE patterns (Fig. 13b). They are all strongly enriched in light REE (251–493 times chondrite for La) relative to HREE (10–27 times chondrite for Yb) with low and almost flat patterns from Ho to Lu. The $(La)_n/(Yb)_n$ ratios of all the magmatic rocks vary between 16.75 and 51.4, of which the trachytes have the lowest ratio between 16.75 and 19.66.

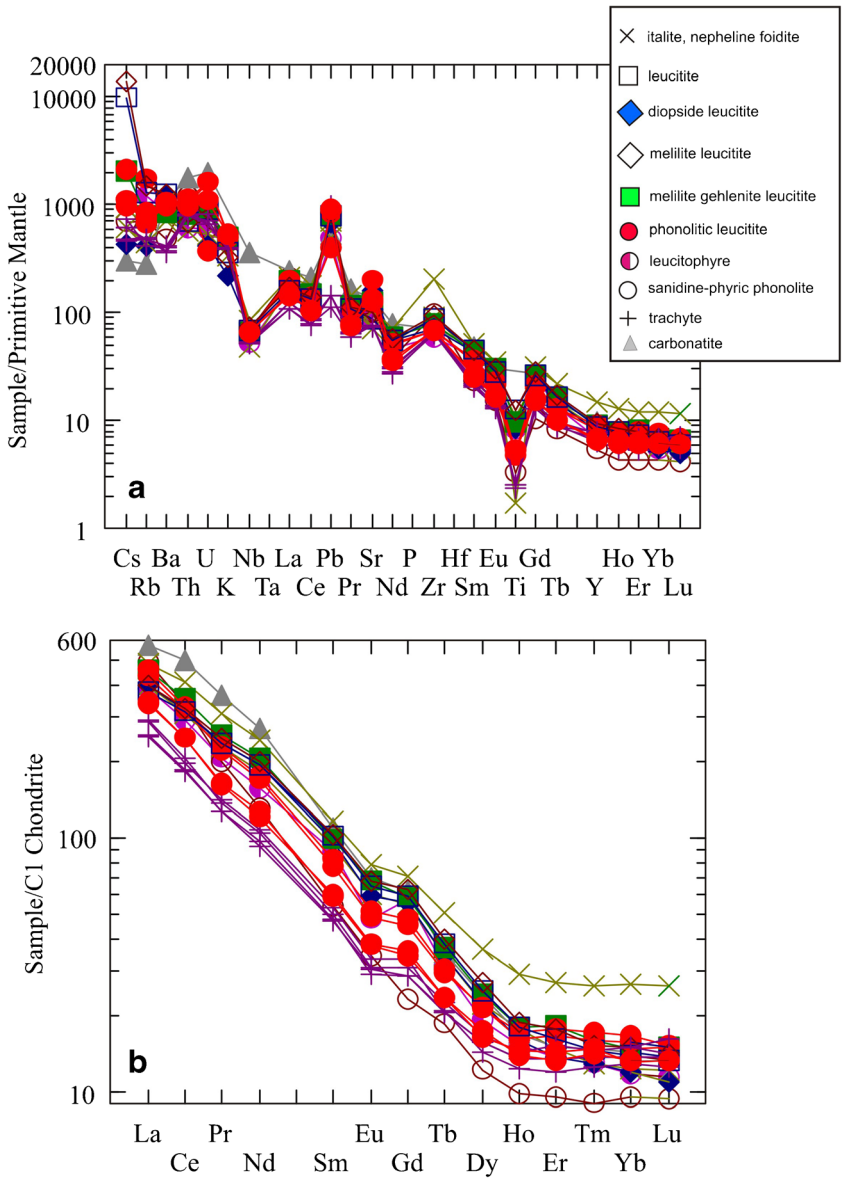

Figs. 13 **a** Primitive mantle-normalized trace element patterns. **b** Chondrite-normalized REE patterns for the potassic, ultrapotassic, and carbonatitic rocks from the study area (normalizing values from Sun and McDonough 1989)

Discussion

Senirkent (Isparta, SW Turkey) and its surrounding area is characterized by potassic and ultrapotassic volcanic rocks and volcano-sedimentary deposits as well as the volcanics from the southern (Gölcük volcano; Alıcı et al. 1998; Platevoet et al. 2008, 2014; Elitok et al. 2010) and northern part of the KAIVP (Francalanci et al. 2000). Ultrapotassic rocks from the study area are leucite-bearing rocks including nepheline-foidolite, italite, leucitite, melilite leucitite, melilite-gehlenite leucitite, diopside leucitite, and leucitophyre. Potassic rocks are phonolitic leucitites, sanidine-phyric phonolite, and trachytes. In general, potassic igneous rocks are classified as calc-alkaline igneous rocks, subduction-related shoshonites, within plate potassic rocks, orogenic ultrapotassic rocks, shoshonitic and alkali lamprophyres (Morrison 1980; Müller and Groves 1997). On the total alkali-silica diagram, majority of ultrapotassic rocks from the study area plot within the foidite area and display positive trend with increasing SiO_2. However, some phonolitic leucitites, leucitophyre, and sanidine-phyric phonolite pass through phonolite and tephriphonolite area (Fig. 11). In other words, they display positive trend with decreasing SiO_2, thought to be related with the carbonate rock-hosted magma chamber processes. On the other hand, potassic and ultrapotassic rocks from the study area display same patterns on the spider diagrams for incompatible elements normalized to the primitive mantle composition. They are characterized by high LILE/HFSE ratio (e.g., strong enrichment in some LILEs such as Cs, Rb, Ba, U, Th, Sr relative to high-field strength elements such as Nb, and Ti), suggesting subduction-related tectonic setting. Morever, they display the

same REE pattern on the chondrite-normalized REE diagram (Fig. 13b) with enrichment in light REE relative to HREE, implying all the rocks are comagmatic. This LREE enrichment could be related to an enriched source (by high-degree metasomatism) or to very low-degree of partial melting in the mantle source. It is strongly suggested that partial melting of garnet peridotite will enrich LREE relative to HREE (Smith and Holm 1990; Zhang et al. 2008) because HREE are preferentially retained in garnet during melting (Anthony et al. 1989; Defant and Drummond 1990; Johnson and Plank 1999; Zhang et al. 2008). However, garnet is identified as a high-pressure indicator mineral in the upper mantle (Haggerty 1995; Johnson and Plank 1999). Therefore, the absence of HREE fractionation is attributed to melting at relatively low pressure, outside the stability field of garnet (Innocenti et al. 1981).

Italite present in the study area is a holocrystalline porphyritic rock with mineral assemblage of leucite, diopside, phlogopite, melanite (Ti-andradite), and apatite minerals. Freda et al. (1997) and Gaeta et al. (2000) linked the presence of Ti-andradite in the italite samples to high P_{CO2} in the magma due to limestone assimilation during emplacement and crystallization. On the other hand, it is commonly reported that due to variation in activities of H_2O and CO_2, different crystallization environments arise in the magma chamber formed within the carbonate rocks. For example, from the Alban Hills Volcanic District, italites were formed near the carbonate contact under elevated CO_2 activity and F-rich phlogopites formed in the inner side of the magma chamber by higher water activity, suggesting increase H_2O/CO_2 from the contact of wall rock to the inner side of magma chamber (Gaeta et al. 2000).

Carbonatite, found as volcaniclastic or associated with potassic magmatic rocks in the study area, is an unusual rock type within the KAIVP. Therefore, this rock type has important signature in terms of understanding evolution of the potassic magmatic rocks in the study area. In general, carbonatites are interpreted to be defined as magmatic rocks with high modal abundance of carbonate minerals (> 50%) and their geochemistry characterized by high abundance of Sr, Ba, P, and LREE (Nelson et al. 1988; Peccerillo 1998; Le Maitre 2002). The composition of the parental magmas of the most carbonatites and the processes they underwent during their emplacement into the crust are still debated. There are three possible mechanisms for the formation of carbonatites: (i) direct melting from carbonate-rich or CO_2-bearing mantle peridotite or wehrlite, (ii) extensive fractional crystallization from alkaline silicate magmas, and (iii) liquid immiscibility in carbonate-silicate magmatic systems (Bailey 1993; Kogarko 1997; De Ignacio et al. 2012 and references therein; Jones et al. 2013 and references therein). On the other hand, Mitchell (2005) discussed that during fractional melting of a carbonated mantle source, there could be extraction of a carbonatite liquid (primary melt: carbonatite-1). With increasing of degree of melting, separate silicate liquid such as a nephelinitic magma could be extracted. If this magma contains carbonate, then it could in turn differentiate into a residual carbonatite and ultimately carbothermal residue (residual melt: carbonatite-2) can be formed. However, he concluded that carbonate-rich rocks formed by pneumatolytic melting of crustal rocks should not be considered carbonatites. The generation of carbonatite melt is likely controlled by the depth (and CO_2 pressure) of the crustal magma chamber, the alkalinity of melts, and the rapidity of magma ascent to the surface (Kogarko 1997).

The main problem for the Senirkent volcanics is whether carbonatite and carbonate-rich rocks represent carbonatitic magma or the carbonates of secondary origin. Based on geological, petrographical, and geochemical data which is consistent with geological, petrological, and laboratory experimental studies for Roman Province magmas (Freda et al. 1997; Iacono Marziano et al. 2007, 2008; Mollo et al. 2010), I reconstruct an eruptive magma system for the magmatic rocks of the northern part of Senirkent, suggesting evidence of uncommon magma evolution process controlled by carbonate assimilation (Fig. 14). Consistently, geological structure of the region is suitable for the process of magma–crustal carbonate wall-rock interaction. Because the study area occurs at the apex of the Isparta Angle consisting of carbonate rock-dominated limbs (Fig. 2). Therefore, it is more plausible that volcanic rocks were formed by way of passing of deep-seated magma through at least a few kilometer-thick carbonate country rocks, hosting extensive source of CO_2. The feeding magma is thought to be interacted with carbonate wall rock, and the magma–carbonate rock interaction processes play a key role on the magma evolution. Peccerillo et al. (2010) suggested that carbonate assimilation occured by reaction between emplaced siliciate magma and solid wall rocks, giving rise to generation of silica-poor and CaO-rich melts. Moreover, immiscible carbonate melts were formed and thermometamorphic calcites took place in the magma. The carbonate melt-related calcites in the studied rocks support this process. Also, Peccerillo (1998) interpreted that strongly undersaturated alkaline rocks are derived from the magma generated at high pressure and X_{CO2}. Crystallization of relatively large leucite should occur under H_2O-undersaturated conditions (Masotta 2012 and references therein). In the study area, italites are associated with carbonatite bearing potassic–ultrapotassic rocks. For the interpretation of italites, it is suggested that ultrapotassic melt emplaced into the carbonate rocks and reacted with the limestones to form thermometamorphic xenoliths. During this reaction, primitive melt assimilated variable amount of limestone. Crystallization of magma at the periphery of the magma chamber produced italite type rocks (Fig. 14). On the other hand, ultrapotassic magma–carbonate rock interaction at the contact give rise to

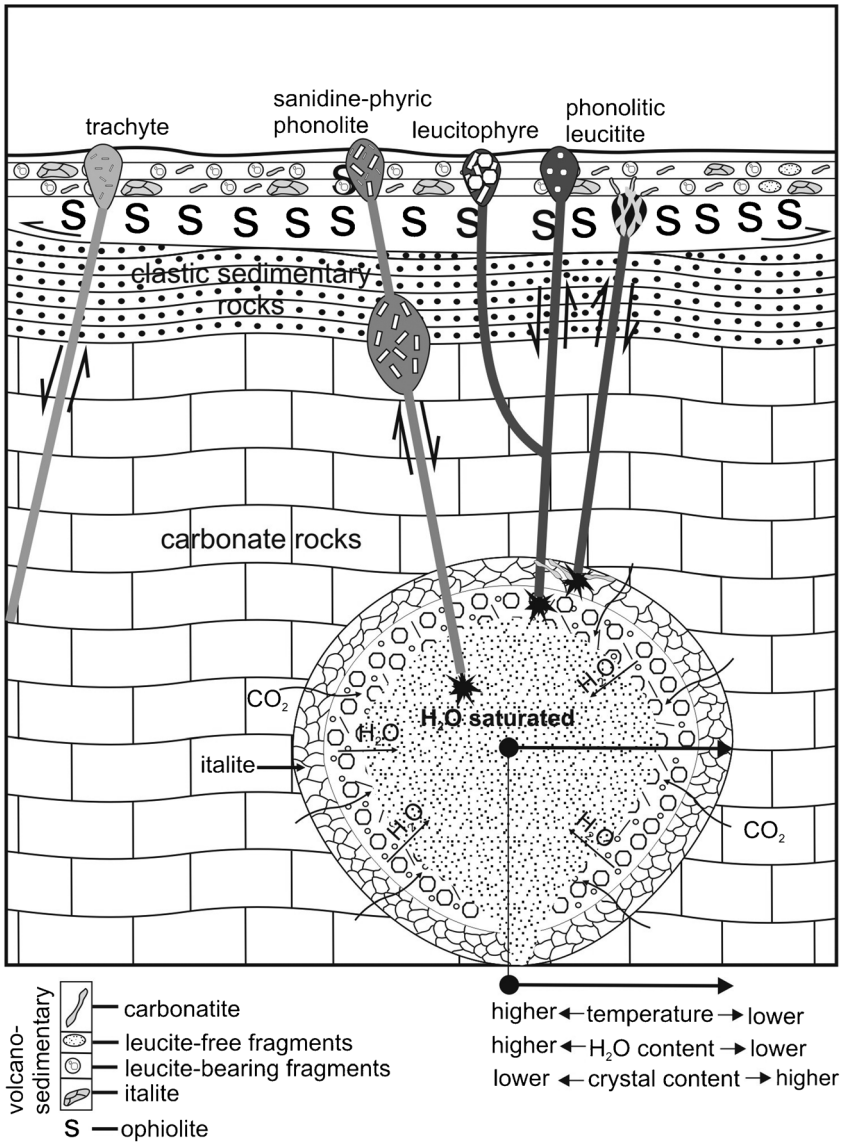

Fig. 14 Schematic drawing that illustrates carbonate rock-hosted magma chamber, magma–carbonate wall-rock interaction processes and multiple eruptions

formation of a Ca-rich sillicate melt that enhances the fractionation of Ca-rich clinopyroxene and supresses the crystallization of plagioclase feldspar and phlogopite in the phonotephritic melts (Cross et al. 2014 and references therein). Based on experimental study on the magma–carbonate interaction, Mollo et al. (2010) explained that carbonate dissolution, by introducing CO_2 in the system, drops water solubility in the melt phase, induces a progressive increase of CO_2/H_2O ratio in the free fluid phase. Hence, the dissolution reaction can be written as (Iacono Marziano et al. 2008):

$$CaCO_3 + MgO^{melt} + 2SiO_2{}^{melt} \rightarrow CaMgSi_2O_6{}^{cpx} + CO_2{}^{fluid}$$

It can be concluded from this reaction that carbonate incorporation into silicate melt causes arising silica-undersaturated melts by consuming SiO_2 to form diopside (Mollo et al. 2010). Temperature and H_2O zoning in the magma chamber could be a factor controlling the degree of crystallization and phase relationships in different sides of the magma chamber. Presence of leucite-free and leucite-bearing lithic fragments within the volcano-sedimentary deposits suggest tapping of different parts of the melts within the magma chamber along the fault lines formed during neotectonic period and extension-related block faulting. Peripheral region of the magma chamber was cooler and H_2O undersaturated allowing crystallization of leucite phenocrysts forming crystalline italite and other leucite-bearing rocks. Extensive magma crystallization and hence increase of H_2O at the periphery of the magma chamber gave rise to H_2O migration toward the inner side of the magma chamber (Fig. 14), where the higher temperature and increasing H_2O content supresses the crystallization of silicate minerals, especially plagioclase crystallization. Consistently, lack of leucite and presence of sanidine in the

sanidine-phyric phonolite testify that H_2O saturation was achieved in the phonolitic melt. There are mainly three groupings on the classification and variation diagrams suggesting that there is a magma storage at different regions and under variable conditions in terms of pressure, temperature, and volatile content. In this respect, most likely except the trachytes, ultrapotassic and phonolitic rocks could be derived from the melts tapped from different sides of the same magma chamber which occured within the carbonate rocks and the melts interacted with carbonate wall rocks (Fig. 14).

Conclusions

- Southwestern Turkey, a complex geodynamic area, is mainly characterized by a carbonate axis forming a north-pointing cusp around Isparta (so-called the Isparta Angle). North-south trending volcanic and/or volcano-sedimentary deposits crop out from the apex of the Isparta Angle (Isparta area) to the north Afyon (Kırka area), called Kırka-Afyon-Isparta Volcanic Province including the study area. Field relations and petrographic and geochemical characteristics of the volcanic rocks from the study area were investigated, and their relationship with carbonatite occurences was discussed.
- On the bases of modal and chemical composition, magmatic rocks of the study area can be classified as (i) leucite-bearing and leucite-free rocks and (ii) potassic and ultrapotassic rocks, respectively. Potassic rocks are phonolitic leucitites, sanidine-phyric phonolite, and trachytes. Ultrapotassic rocks are nepheline-foidolite, italite, leucitite, melilite leucitite, melilite-gehlenite leucitite, diopside leucitite, and leucitophyre. Carbonatitic calcite occurences can be observed within some leucitites, diopside leucitites, phonolitic leucitites. Furthermore, carbonate-rich part including carbonatite globules, phlogopite, clinopyroxene and/or leucite, melanite crystals embedded in glassy volcanic matrix and/or carbonate matrix can be associated with these rocks. Plagioclase is absent in all leucite-bearing and leucite-free rocks.
- Potassic rocks are characterized with SiO_2 (49.35–64.46 wt%), K_2O (8.28–11.38 wt%), MgO (0.17–1.39 wt%), and K_2O/Na_2O ratio (2.25–11.8). Ultrapotassic rocks are characterized with the lowest SiO_2 content (38.71–44.72 wt%, but the leucitophyre has 51.4 wt%), higher K_2O (4.36–10.19 wt%), MgO (3.25–6.98 wt%), and K_2O/Na_2O ratio (2.65–32.8). Ultrapotassic, phonolitic rocks, and trachytes have Ba content (3612–6438; 2457–5321; 1826–2104 ppm), Sr (1282–2901; 1792–3509; 1292–1376 ppm), and Rb (232.6–831.3; 369.7–947.8; 227.7–274.9 ppm), respectively. On the total alkali-silica diagram, majority of ultrapotassic rocks from the study area plot within the foidite area and display positive trend with increasing SiO_2. However, some phonolitic leucitites, leucitophyre, sanidine-phyric phonolite show positive trend with decreasing SiO_2, thought to be related with the carbonate rock-hosted magma chamber processes.
- On the primitive mantle-normalized incompatible element patterns, they are characterized by high LILE/HFSE ratio (e.g., strong enrichment in some LILEs such as Cs, Rb, Ba, U, Th, Sr relative to HFSE such as Nb, and Ti), suggesting subduction-related tectonic setting. Chondrite-normalized REE patterns display light REE enrichment (251–493 times chondrite for La) and flat heavy REE patterns (10–27 times chondrite for Yb). All the leucite-bearing and leucite-free rocks display similar, subparallel chondrite-normalized and primitive mantle-normalized trace element patterns, suggesting cogenetic origin.
- Based on mineralogical, petrological, and geochemical data, it is suggested that ultrapotassic and phonolitic rocks, except the trachytes, could be derived from the melts tapped from different sides of the same magma chamber occured within the carbonate rocks and the melts interacted with carbonate wall rocks.

Funding This work was funded by the Süleyman Demirel University Research Foundation (Project no. 1994-YL-09).

References

Akal C (2003) Mineralogy and geochemistry of Melilite Leucitites, Balçıkhisar, Afyon (Turkey). Turk J Earth Sci 12:215–239

Akal C (2008) K-richterite-olivine-phlogopite-diopside-sanidine lamproites from the Afyon province, Turkey. Geol Mag 145:570–585

Akal C, Helvacı C, Prelević D, van den Bogaard P (2013) High-K volcanism in the Afyon region, western Turkey: from Si-oversaturated to Si-undersaturated volcanism. Int J Earth Sci 102:435–453

Alıcı P, Temel A, Gourgaud A, Kieffer G, Gündoğdu MN (1998) Petrology and geochemistry of the potassic rocks in the Gölcük area (Isparta, SW Turkey): genesis of enriched alkaline magmas. J Volcanol Geotherm Res 85:423–446

Allen M, Jackson J, Walker R (2004) Late Cenozoic reorganization of the Arabia–Eurasia collision and the comparison of short-term and long-term deformation rates. Tectonics 23:TC2008. https://doi.org/10.1029/2003TC001530

Anthony EY, Segalstad TV, Neumann E-R (1989) An unusual source region for nephelinites from the Oslo Rift, Norway. Geochim Cosmochim Acta 53:1067–1076

Aydar E, Bayhan H, Gourgaud A (2003) The lamprophyres of Afyon stratovolcano, western Anatolia, Turkey: description and genesis. Geoscience 335:279–288

Bailey DK (1993) Carbonate magmas. J Geol Soc London 150:637–651

Balcı V (2011) 1/100 000 ölçekli Türkiye Jeoloji Haritaları, Afyon-L25 paftası: Maden Tetkik ve Arama Genel Müdürlüğü, Jeoloji Etüdleri Dairesi Yayını No:161, Ankara, Türkiye

Barazangi M, Sandvol E, Seber D (2006) Structure and tectonic evolution of the Anatolian plateau in eastern Turkey. In: Dilek Y, and Pavlides S (eds) Post-collisional tectonics and magmatism in the eastern Mediterranean region and Asia, Geol Soc Spec Pap 409:463–474

Beccaluva L, Di Girolama P, Serri G (1991) Petrogenesis and tectonic setting of the Roman Volcanic Province, Italy. Lithos 26:191–221

Becker-Platen JD, Benda L, Steffens P (1977) Lithound biostratigraphische Deutung radiometrischer altersbestimmungen au dem jungtertlar der Turkei (Kanozoikum und Braunkohlen edr Turkei, 18). Geol Jb B25:139–167

Bingöl E (1989) 1/2 000 000 ölçekli Türkiye Jeoloji Haritası. Maden Tetkik ve Arama Genel Müdürlüğü, Jeoloji Etüdleri Dairesi, Ankara, Türkiye

Bozkurt E (2001) Neotectonics of Turkey—a synthesis. Geodin Acta 14: 3–30

Büyüksaraç A (2007) Investigation into the regional wrench tectonics of inner East Anatolia (Turkey) using potential field data. Phys Earth Planet Inter 160:86–95

Cioni R, Marianelli P, Santacroce R (1998) Thermal and compositional evolution of the shallow magma chambers of Vesuvius: evidence from pyroxene phenocrysts and melt inclusions. J Geophys Res 103(B8):18277–18294

Çoban H, Bozcu M, Yılmaz K (2003) Sandıklı-Şuhut (Afyon) güneyi ultrapotasik volkanitlerinin petrojenezi. Süleyman Demirel Üniversitesi, Fen Bilimleri Enstitüsü Dergisi (Özel Sayı) 7(2):179–188

Comin-Chiaramonti P, Gomes CB, Cundari A, Castorina F, Censt P (2007) A review of carbonatitic magmatism in the Parana-Angola-Namibia (PAN) system. Period Mineral, Special Issue 76(2–3):25–78

Cross JK, Tomlinson EL, Giordano G, Smith VC, De Benedetti AA, Roberge J, Manning CJ, Wulf S, Menzies MA (2014) High level triggers for explosive mafic volcanism: Albano Maar, Italy. Lithos 190–191:137–153

De Ignacio C, Muñoz M, Sagredo J (2012) Carbonatites and associated nephelinites from São Vicente, Cape Verde Islands. Mineral Mag 76(2):311–355

Defant M, Drummond M (1990) Derivation of some modern arc magmas by melting of young subducted lithosphere. Nature 347:662–665

Dewey JF, Hempton MR, Kidd WSF, Şaroğlu F, Şengör AMC (1986) Shortening of continental lithosphere: the neotectonics of Eastern Anatolia—a young collision zone. In: Coward MP, Ries AC (eds) Collision tectonics (J Geol Soc London Spec Publ) 19:3–36

Dilek Y, Moores EM (1990) Regional tectonics of the eastern Mediterranean ophiolites. In: Malpas J, Moores EM, Panayiotou A, Xenophontos C (eds) Ophiolites, oceanic crustal analogues. Proceedings of the Symposium "Troodos 1987". Geological Survey Department, Nicosia, Cyprus, pp 295–309

Dilek Y, Furnes H, Shallo M (2007) Suprasubduction zone ophiolite formation along the periphery of Mesozoic Gondwana. Gondwana Res 11:453–467

Elitok Ö, Özgür N, Drüppel K, Dilek Y, Platevoet B, Guillou H, Poisson A, Scaillet S, Satır M, Siebel W, Bardintzeff J-M, Deniel C, Yılmaz K (2010) Origin and geodynamic evolution of late Cenozoic alkali potassium-rich volcanism in Isparta area, SW Turkey. Int Geol Rev 52(4–6):454–504

Erişen B (1972) Afyon-Heybeli (Kızılkilise) jeotermal araştırma sahasının jeolojisi ve jeotermal olanakları. Maden Tetkik Arama Enstitüsü Raporu, No:3107, (unpublished), Ankara, Türkiye

Foley SF, Venturelli G, Green DH, Toscani L (1987) The ultrapotassic rocks: characteristics, classification, and constraints for petrogenetic models. Earth Sci Rev 24:81–134

Francalanci L, Innocenti F, Manetti P, Savasçın MY (2000) Neogene alkaline volcanism of the Afyon-Isparta area, Turkey: petrogenesis and geodynamic implications. Mineral Petrol 70:285–312

Freda C, Gaeta M, Palladino D, Trigila R (1997) The Villa Senni eruption (Alban Hills, Central Italy): the role of H_2O and CO_2 on the magma chamber evolution and onthe eruptive scenario. J Volcanol Geotherm Res 78:103–120

Gaeta M, Gabrizio G, Cavarretta G (2000) F-phlogopites in the Alban Hills Volcanic District (Central Italy): indications regarding the role of volatiles in magmatic crystallisation. J Volcanol Geotherm Res 99:179–193

Gürer ÖF, Gürer A (1999) Development of evaporites and the counter-clockwise rotation of Anatolia, Turkey. Int Geol Rev 41:607–622

Haggerty SE (1995) Upper mantle mineralogy. J Geodyn 20(4):331–364

Hubert-Ferrari A, King G, Manighetti I, Armijo R, Meyer B, Tapponnier P (2003) Long-term elasticity in the continental lithosphere; modelling the Aden ridge propagation and the Anatolian extrusion process. Geophys J Int 153:111–132

Iacono Marziano G, Gaillard F, Pichavant M (2007) Limestone assimilation and the origin of CO_2 emissions at the Alban Hills (Central Italy): constraints from experimental petrology. J Volcanol Geotherm Res 166:91–105

Iacono Marziano G, Gaillard F, Pichavant M (2008) Limestone assimilation by basaltic magmas: an experimental re-assessment and application to Italian volcanoes. Contrib Mineral Petrol 155:719–738

İnal A (1975) Afyon bölgesi gölsel Neoje'ninde bulunmuş yeni iki Gastropod türü ve bir alt tanımı. Türk Jeol Kurumu Bül 18(2): 161–164

Innocenti F, Manetti P, Peccerillo A, Poli G (1981) South Aegean volcanic arc: geochemical variations and geotectonic implications. Bull Volcanol 44(3):377–391

Johnson MC, Plank T (1999) Dehydration and melting experiments constrain the fate of subducted sediments. Geochem Geophys Geosys 1(1):1007. https://doi.org/10.1029/1999GC000014 ISSN:1525-2027

Jones AP, Genge M, Carmody L (2013) Carbonate melts and carbonatites. Rev Mineral Geochem 75:289–322

Juteau T (1980) Ophiolites of Turkey. Ofioliti 2:199–237

Koçyiğit A (1984a) Güneybatı Türkiye ve yakın dolayında levha içi yeni tektonik gelişim. Türk Jeol Kurumu Bül 27:1–16

Koçyiğit A (1984b) Tectono-stratigraphic characteristics of Hoyran Lake region (Isparta Bend). In: Tekeli O, Göncüoğlu MC (eds) Geology of the Taurus Belt. Proceedings, MTA, Ankara, Turkey, pp 53–67

Koçyiğit A, Yılmaz A, Adamia A, Kuloshvili S (2001) Neotectonics of east Anatolian plateau (Turkey) and lesser Caucasus: implication for transition from thrusting to strike-slip faulting. Geodin Acta 14:177–195

Kogarko NL (1997) Role of CO_2 on differentiation of ultramafic alkaline series: liquid immiscibility in carbonate-bearing phonolitic dykes (Polar Siberia). Mineral Mag 61:549–556

Le Bas MJ, Le Maitre RW, Streckeisen A, Zanettin B (1986) A chemical classification of volcanic rocks based on the total alkali–silica diagram. J Petrol 27(3):745–750

Le Maitre RW (2002) Igneous rocks: a classification and glossary of terms. Cambridge University Press, Cambridge 236 p

Lefèvre C, Bellon H, Poisson A (1983) Présences de leucitites dans le volcanisme Pliocéne de la région d'Isparta (Taurides occidentales, Turquie). C R Acad Sci Hebd Seances Acad Sci D 297(2):367–372

Masotta M (2012) Magma differentiation in shallow, thermally zoned magma chamber: the example of Sabatini volcanic district (Central Italy). Plinius 38:119–126

McClusky S, Balassanian S, Barka A, Demir C, Ergintav S, Georgiev I, Gurkan O, Hamburger M, Hurst K, Kahle H, Kastens K, Kekelidze G, Ring R, Kotzev V, Lenk O, Mahmoud S, Mishin A, Nadariya M, Ouzounis A, Paradissis D, Peter Y, Prilepin M, Reilinger R, Sanli I, Seeger H, Tealeb A, Toksöz MN, Veis G (2000) Global positioning system constraints on plate kinematics and dynamics in the eastern Mediterranean and Caucasus. J Geophys Res Solid Earth 105:5695–5719

Mitchell RH (2005) Carbonatites and carbonatites and carbonatites. Can Mineral 43:2049–2068

Mollo S, Gaeta M, Freda C, Di Rocco T, Misiti V, Scarlato P (2010) Carbonate assimilation in magmas: a reappraisal based on experimental petrology. Lithos 114:503–514

Morrison GW (1980) Characteristics and tectonic setting of the shoshonite rock association. Lithos 13:97–108

Müller D, Groves DI (1997) Potassic igneous rocks and associated gold–copper mineralization. Springer Verlag, Berlin, p 252

Nelson DR (1992) Isotopic characteristics of potassic rocks: evidence for the involvement of subducted sediments in magma genesis. Lithos 28:403–420

Nelson DR, Chivas AR, Chappell BW, McCulloch MT (1988) Geochemical and isotopic systematics in carbonatites and implications for the evolution of ocean-island sources. Geochim Cosmochim Acta 52:1–17

Özçep F, Orbay N (2000) Paleomagnetic studies on the Anatolian (Turkish) plate and geodynamic implications: a review. Terra Nostra 10, From Secular Variation to Paleomagnetism-Workshop, Potsdam, pp 93–94

Pearce JA (1982) Trace element characteristics of lavas from destructive plate boundaries. In: Thorpe RS (ed) Andesites. Wiley, New York, pp 525–548

Pearce JA (1983) Role of the sub-continental lithosphere in magma genesis at active continental margins. In: Hawkesworth CJ, Norry NJ (eds) Continental basalts and mantle xenoliths. Shiva, Cheshire, pp 230–249

Pearce JA, Cann JR (1973) Tectonic setting of basic volcanic rocks determined using trace element analyses. Earth Planet Sci Lett 19:290–300

Pearce JA, Norry MJ (1979) Petrogenetic implications of Ti, Zr, Y, and Nb variations in volcanic rocks. Contrib Mineral Petrol 69(1):33–47

Pearce JA, Peate DW (1995) Tectonic implications of the composition of volcanic arc magmas. Annu Rev Earth Planet Sci 23:251–285

Peccerillo A (1998) Relationships between ultrapotassic and carbonate-rich volcanic rocks in Central Italy: petrogenetic and geodynamic implications. Lithos 43:267–279

Peccerillo A, Poli G, Tolomeo L (1984) Genesis, evolution and tectonic significance of K-rich volcanics from the Alban Hills (Roman comagmatic region) as inferred from trace element geochemistry. Contrib Mineral Petrol 86:230–240

Peccerillo A, Federico M, Barbieri M, Brilli M, Wu T-W (2010) Interaction between ultrapotassic magmas and carbonate rocks: evidence from geochemical and isotopic (Sr, Nd, O) compositions of granular lithic clasts from the Alban Hills Volcano, Central Italy. Geochim Cosmochim Acta 74:2999–3022

Pichavant M, Scaillet B, Pommier A, Iacono Marziano G, Cioni R (2014) Nature and evolution of primitive vesuvius magmas: an experimental study. J Petrol 55(11):2281–2310

Platevoet B, Scaillet S, Guillou H, Blamart D, Nomade S, Massault M, Poisson A, Elitok Ö, Özgür N, Yağmurlu F, Yılmaz K (2008) Pleistocene explosive activity of the Gölcük volcano, Isparta Angle. Turkey Quaternaire 19(2):147–156

Platevoet B, Elitok Ö, Guillou H, Bardintzeff J-M, Yagmurlu F, Nomade S, Poisson A, Deniel C, Özgür N (2014) Petrology of quaternary volcanic rocks and related plutonic xenoliths from Gölcük volcano, Isparta angle, Turkey: origin and evolution of the high-K alkaline series. J Asian Earth Sci 92:53–76

Platzman ES, Tapırdamaz C, Sanver M (1998) Neogene anticlockwise rotation of Central Anatolia (Turkey): preliminary paleomagnetic and geochronological results. Tectonophysics 299:175–189

Poli G, Frey FA, Ferrara G (1984) Geochemical characteristics of the South Tuscany (Italy) volcanic province: constraints on lava petrogenesis. Chem Geol 43:203–221

Reilinger RE, McClusky SC, Oral MB, King W, Toksöz MN, Barka AA, Kınık I, Len O, Sanli I (1997) Global positioning system measurements of present-day crustal movements in the Arabian–Africa–Eurasia plate collision zone. J Geophys Res Solid Earth 102:9983–9999

Saunders AD, Tarney J, Weaver SD (1980) Transverse geochemical variations across the Antarctic peninsula: implications for the genesis of calc-alkaline magmas. Earth Planet Sci Lett 46:344–360

Savaşçın MY, Oyman T (1998) Tectono-magmatic evolution of alkaline volcanics at the Kırka–Afyon–Isparta structural trend, SW Turkey. Turk J Earth Sci 7:201–214

Schmitt AK, Danišík M, Siebel W, Elitok Ö, Chang Y-W, Shen C-C (2014) Late Pleistocene zircon ages for intracaldera domes at Gölcük (Isparta, Turkey). J Volcanol Geotherm Res 286:24–29

Şengör AMC (1979) The North Anatolian transform fault: its age, offset and tectonic significance. J Geol Soc 136:269–282

Şengör AMC, Yılmaz Y (1981) Tethyan evolution of Turkey: a plate tectonic approach. Tectonophysics 75:181–241

Şengör AMC, Görür N, Şaroğlu F (1985) Strike-slip faulting and related basin formation in zones of tectonic escape: Turkey as a case study. In: Biddle KT, Christie-Blick N (eds) Strike-slip deformation, basin formation and sedimentation (Society of Economic Mineralogist and Paleontologists, Spec Publ) 37:227–264

Shaw CSJ (2018) Evidence for the presence of carbonate melt during the formation of cumulates in the Colli Albani Volcanic District, Italy. Lithos 310-311:105–119

Shervais JW (1982) Ti–V plots and the petrogenesis of modern and ophiolitic lavas. Earth Planet Sci Lett 59(1):101–118

Smith TE, Holm PE (1990) The petrogenesis of mafic minor intrusions and volcanics of the Central Metasedimentary Belt, Grenville Province, Canada: MORB and OIB sources. Precambrian Res 48: 361–373

Sun SS, McDonough WF (1989) Chemical and isotopic systematics of oceanic basalts: implications for mantle composition and processes. In: Saunders AD, Norry MJ (eds) Magmatism in ocean basins (Jour Geol Soc London Spec Publ) 42:313–347

Tatar O, Piper JDA, Gürsoy H, Temiz H (1996) Regional significance of neotectonic counterclockwise rotation in Central Turkey. Int Geol Rev 38:692–700

Van Bergen MJ, Vroon PZ, Varekamp JC, Poorter RPE (1992) The origin of the potassic rock suite from Batu Tara volcano (East Sunda Arc, Indonesia). Lithos 28:261–282

Wooley AR (2003) Igneous silicate rocks associated with carbonatites: their diversity, relative abundances and implications for carbonatite genesis. Per Mineral Spec Issue 72:9–17

Zhang Z, Xiao X, Wang J, Wang Y, Musky TM (2008) Post-collisional Plio-Pleistocene shoshonitic volcanism in the western Kunlun Mountains, NW China: geochemical constraints on mantle source characteristics and petrogenesis. J Asian Earth Sci 31:379–403